Highly resolved mapping of NO_2 vertical column densities from GeoTASO measurements over a megacity and industrial area during the KORUS-AQ campaign

Gyo-Hwang Choo[1], Kyunghwa Lee[1], Hyunkee Hong[1*], Ukkyo Jeong[2,3], Wonei Choi[4], Scott J. Janz[3]

[1]Environmental Satellite Center, National Institute of Environmental Research, Hwangyeong-ro 42, Seo-gu, Incheon, Republic of Korea, 22689
[2]Earth System Science Interdisciplinary Center, University of Maryland, College Park, Maryland, USA 20740
[3]NASA Goddard Space Flight Center, Greenbelt, Maryland, USA, 20771
[4]Division of Earth Environmental System Science, Major of Spatial Information Engineering, Pukyong National University, Busan 48513, South Korea

Correspondence to: Hyunkee Hong; Tel: +82 32 560 8437; Fax: +82 32 560 8460; E-mail address: wanju77@korea.kr

Abstract. The Korea-United States Air Quality (KORUS-AQ) campaign is a joint study between the United States National Aeronautics and Space Administration (NASA) and the South Korea National Institute of Environmental Research (NIER) to monitor megacity and transboundary air pollution around the Korean Peninsula using airborne and ground-based measurements. Here, tropospheric nitrogen dioxide (NO_2) slant column density (SCD) measurements were retrieved from Geostationary Trace and Aerosol Sensor Optimization (GeoTASO) L1B data during the KORUS-AQ campaign (May 2 to June 10, 2016). The retrieved SCDs were converted to tropospheric vertical column densities using the air mass factor (AMF) obtained from a radiative transfer calculation with trace gas profiles and aerosol property inputs simulated with the Community Multiscale Air Quality (CMAQ) model and surface reflectance data obtained from the Moderate Resolution Imaging Spectroradiometer (MODIS). For the first time, we examine highly resolved (250 m × 250 m resolution) tropospheric NO_2 over the Seoul and Busan metropolitan regions, and the industrial regions of Anmyeon. We reveal that the maximum NO_2 VCDs were 4.94×10^{16} and 1.46×10^{17} molecules cm^{-2} at 9 AM and 3 PM over Seoul, respectively, 6.86×10^{16} and 4.89×10^{16} molecules cm^{-2} in the morning and afternoon over Busan, respectively, and 1.64×10^{16} molecules cm^{-2} over Anmyeon. The VCDs retrieved from the GeoTASO airborne instrument were correlated with those obtained from the Ozone Monitoring Instrument (OMI) ($r = 0.48$), NASA's Pandora Spectrometer System ($r = 0.91$), and NO_2 mixing ratios obtained from in situ measurements ($r = 0.07$ in the morning, $r = 0.26$ in the afternoon over the Seoul, and $r > 0.56$ over Busan). Based on our results, GeoTASO is useful for identifying NO_2 hotspots and their spatial distribution in highly populated cities and industrial areas.

1 Introduction

Nitrogen dioxide (NO_2) is one of the most important atmospheric trace gases and plays a key role in aerosol production and tropospheric ozone photochemistry (Boersma et al., 2004; Richter et al., 2005). Furthermore, high concentrations of NO_2 in the atmosphere have adverse effects on human health, such as respiratory infections, and associated symptoms (Brauer et al., 2002; Latza et al., 2009).

The main sources of NO_2 in the atmosphere are fossil fuel combustion from vehicles and thermal power plants, lightning, and biogenic soil processes. Furthermore, NO_2 concentrations are highly correlated with population size (Lamsal et al., 2013). The implementation of emission control technology and environmental regulation has led to a decrease in surface NO_2 concentrations in Western Europe, the United States, and Japan in the last few decades (Richter et al., 2005). The concentration of NO_2 in major metropolitan cities in South Korea and China is over 3 times larger than over similarly sized cities in Europe and United States, despite NO_2 concentration decreasing in China and South Korea (de Foy et al., 2016, Choo et al., 2020).

To date, several low-orbit space borne sensors, such as the Global Ozone Monitoring Experiment (GOME) (Burrows et al., 1999), the Scanning Imaging Spectrometer for Atmospheric Cartography (SCIAMACHY) (Burrows et al., 1995), the Ozone

Monitoring Instrument (OMI) (Levelt et al., 2006), the GOME-2 (Callies et al., 2000), and the Tropospheric Monitoring Instrument (TROPOMI) (Veefkind et al., 2012), have monitored atmospheric ozone and its precursors including NO_2 and formaldehyde (HCHO) as a proxy for volatile organic compounds (VOCs). Furthermore, the Geostationary Environment Monitoring Spectrometer (GEMS) (Choi et al., 2018; Kim et al., 2020), which was launched on February 18, 2020, will form a constellation of geostationary satellites including the upcoming Tropospheric Emission: Monitoring of Pollution (TEMPO) (Zoogman et al., 2017) and Sentinel-4 platforms, to continuously observe the air quality of the Northern Hemisphere during the day.

NO_2 retrievals from space borne hyperspectral measurements are typically conducted using the differential optical absorption spectroscopy (DOAS) method (Platt and Stutz, 2008) to first retrieve the view-dependent slant column density (SCD), and then radiative transfer models are used to determine the vertical column density (VCD) using an air mass factor (AMF) correction. Previous and ongoing space borne instruments use various radiative transfer codes and model input assumptions to calculate NO_2 AMF values at coarse spatial resolution. Because AMF weighting has a large impact on NO_2 retrievals using the DOAS method, it is important to use model input assumptions that most accurately match viewing and atmospheric conditions. Several studies have demonstrated the sensitivity of AMF calculations to inaccurate model input parameters (e.g., *a priori* NO_2 vertical profile and aerosol properties) and *a priori* data (cloud information and surface reflectance) (Leitão et al., 2010; Hong et al., 2017; Lorente et al., 2017; Boersma et al., 2018). NO_2 retrievals have also been consistently conducted based on surface remote sensing measurements including the Multi-Axis DOAS (MAX-DOAS), Système D'Analyse par Observations Zènithales (SAOZ) spectrometer (Pastel et al., 2014), and Pandora (Herman et al., 2009) systems. These ground-based measurements can be used as validation references for both airborne and space borne measurements.

NO_2 retrievals from airborne remote sensing instruments, such as the Geostationary Coast and Air Pollution Event (GEO-CAPE) Airborne Simulator (GCAS) (Kowalewski and Janz, 2014), the Heidelberg Airborne Imaging DOAS Instrument (HAIDI) (General et al., 2014), the Geostationary Trace gas and Aerosol Sensor Optimization (GeoTASO) (Leitch et al., 2014), the Airborne Prism Experiment (APEX; Popp et al., 2012), the Airborne Imaging DOAS instrument for Measurements of Atmospheric Pollution (AirMAP; Meier et al., 2017; Schönhardt et al., 2015), the Small Whiskbroom Imager for atmospheric compositioN monitorinG (SWING; Merlaud et al. 2018), and the Spectrolite Breadboard Instrument (SBI; Vlemmix et al., 2017; Tack et al., 2019) have also been performed to identify local emission sources and obtain highly resolved horizontal NO_2 distributions.

Observations using airborne measurements have an advantage as they enable the observation of horizontal distributions of trace gases at resolutions higher than those of space-based satellites and provide data over a wider area than those of ground-based observations. For example, Nowlan et al. (2018) retrieved tropospheric NO_2 VCDs over Houston, Texas, during the Deriving Information on Surface Conditions from Column and Vertically Resolved Observations Relevant to Air Quality (DISCOVER-AQ) campaign and identified a high correlation with data retrieved from Pandora. Popp et al. (2012) also presented the morning and afternoon NO_2 spatial distribution in Zurich, Switzerland, using APEX. Tack et al. (2017) have conducted high-resolution mapping of NO_2 over three Belgium cities (Antwerp, Brussels, and Liège) using APEX and Judd et al. (2020) and Tack et al. (2021) compared NO_2 VCDs retrieved from GCAS/GeoTASO and APEX with those obtained from TROPOMI over New York City and Antwerp and Brussels, respectively. Merlaud et al. (2013) observed NO_2 VCDs in Turceni over Romania using SWING mounted on an unmanned aerial vehicle (UAV) during the Airborne Romanian Measurements of Aerosols and Trace gases (AROMAT) campaign. These existing NO_2 retrievals, using airborne measurements, have been useful in constraining regional air quality models due to the highly resolved source identification and the ability to tie these results to ground-based observations.

This work focuses on airborne NO_2 retrievals from GeoTASO. This instrument was developed by Ball Aerospace to reduce mission risk for UV-VIS air quality measurements from geostationary orbit for the GEMS and TEMPO missions (Leitch et al., 2014). The retrieval of NO_2, SO_2, and HCHO observed from GeoTASO L1B data using DOAS and principal component analysis (PCA) (Wold et al., 1987) was conducted through the DISCOVER-AQ and KORea-United States Air Quality (KORUS-AQ) campaigns (Nowlan et al., 2016; Judd et al., 2018; Choi et al., 2020; Chong et al., 2020). The KORUS-AQ campaign is a joint study between the National Institute of Environmental Research (NIER) and National Aeronautics and Space Administration (NASA) to monitor megacity air pollution and transboundary pollution, and to prepare for geostationary satellite (i.e., GEMS, TEMPO, and Sentinel-4) air quality observability (of trace gases and aerosols), organized from May to June 2016.

Although surface NO_2 concentrations in South Korea are the high due to high population density, high traffic volumes, and many industrial complexes and thermal power plants, and although NO_2 retrieval studies using airborne and ground measurements in North America, Europe, China, and Japan, data for South Korea remain limited. The specific objectives of this study are as follows:

(1) To retrieve tropospheric NO_2 vertical column data using GeoTASO measurements over polluted regions of the Seoul and Busan metropolitan areas and the Anmyeon industrial regions of the Korean Peninsula.

(2) To estimate NO_2 VCD uncertainties using error propagation accounting for spectral fitting errors and AMF uncertainties associated with input data errors, including aerosol optical depth (AOD), single scattering albedo (SSA), aerosol peak height (APH), and surface reflectance (SRF).

(3) To compare NO_2 VCDs retrieved from GeoTASO and those obtained from OMI and ground-based Pandora instruments, as well as surface in situ measurements.

2 KORUS-AQ campaign area, measurements, and model simulation

2.1 Campaign area

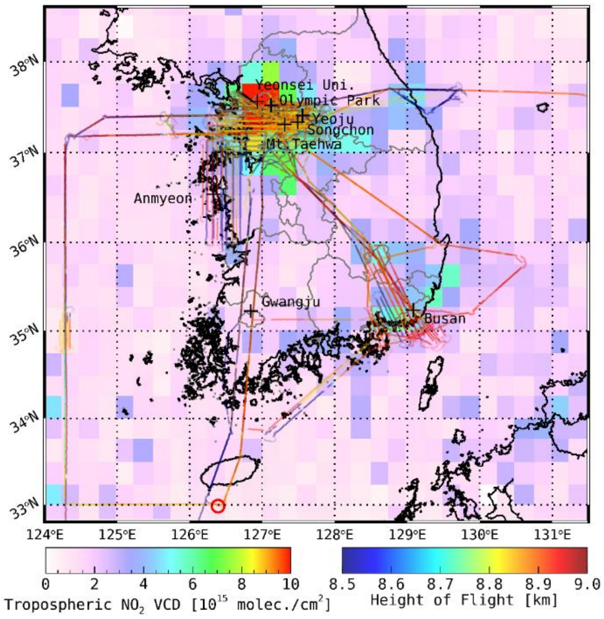

Figure 1. Flight paths of the NASA LaRC B200 aircraft carrying GeoTASO and the average tropospheric NO_2 VCDs obtained from OMI gridded to a 0.25° × 0.25° horizontal grid during the KORUS-AQ campaign period. The line color represents flight height. In this period, the GeoTASO observations focused on megacities (Seoul and Busan) and industrial complex area (Anmyeon) with high tropospheric NO_2 concentrations. The reference spectrum for spectral fitting is obtained from the radiation data over the Jeju Island (marked with red circle).

The Korean Peninsula, located on the Asia-Pacific coast, has a complex atmospheric environment by local emissions and long-range transport under appropriate weather conditions (Jeong et al., 2017; NIER and NASA, 2020; Choo et al., 2021). Seoul, the capital of South Korea, and the metropolitan area are densely populated, and power plants and industrial activities on the northwest coast are conducted, which emit relatively large amounts of pollutants. The KORUS-AQ campaign conducted three-dimensional observations, including ground-based remote, aircraft, satellite observation, and air quality modeling, to understand the complex air quality and interpret the observations of GEMS launched in 2020. The KORUS-AQ campaign period was from May 2 to June 10, 2016. During the KORUS-AQ campaign, air pollutants were conducted using the GeoTASO on board the NASA Langley Research Center B200 aircraft to monitor air quality and long-range transport of pollutants over the Korean Peninsula (NIER and NASA, 2020). The GeoTASO observations were conducted 30 times in 23 d out of 40 d. Most observations were made once or twice a day. Each flight was planned and conducted on a day when the weather conditions were fine and flight hours were approximately 2-4 h. We show the average values of GeoTASO flight information such as flight time, altitude, speed, solar zenith angle (SZA), and viewing zenith angle (VZA) for the dates retrieved for NO_2 VCD, aerosol properties (AOD, SSA) extracted from CMAQ, and cloud fraction and surface reflectance extracted from the Moderate Resolution Imaging Spectroradiometer (MODIS) in Table 1. Flight information on the date of aircraft observation can be found at http://www-air.larc.nasa.gov/missions/korus-aq/docs/KORUS-AQ_Flight_Summaries_ID122.pdf. Figure 1 indicates the flight routes of B200 and the tropospheric NO_2 VCD obtained from the OMI during the campaign period. The observations were concentrated in the metropolitan areas of Seoul and Busan and the industrial areas of Anmyeon, with an average flight altitude of ~8.5 km during KORUS-AQ.

Table 1. Summary of information on the dates when NO_2 VCD was retrieved during the KORUS-AQ period (LT = UTC + 9 h). The average values of GeoTASO data sets for flight characteristics, aerosol properties, geometric information and cloud information.

Date	**Jun 5**	**Jun 9 AM**	**Jun 9 PM**	**Jun 10 AM**	**Jun 10 PM**
ROI	Anmyeon	Seoul metropolitan		Busan metropolitan	
Flight time (LT)	13:11–17:20	7:48–12:00	13:46–17:52	8:02–11:38	13:05–15:19
Flight altitude (km)	8.6	8.4	8.5	8.6	8.5
Flight speed (km hr^{-1})	117.0	116.2	117.6	117.2	117.1
SZA (°)	39.2	36.1	45.3	35.9	33.0
VZA (°)	11.9	12.6	12.8	12.1	11.8
AOD	0.27	0.40	0.21	0.13	0.09
SSA	0.966	0.980	0.949	0.981	0.968
Surface reflectance	0.07	0.09	0.09	0.06	0.06

Cloud fraction	0.08	0.31	0.55	0.16	0.20

As shown in Fig. 1, GeoTASO observations were conducted focusing on highly NO_2-polluted regions in the Seoul and Busan metropolitan areas and the Anmyeon region during the KORUS-AQ campaign. The Seoul metropolitan area (Seoul Special City, Gyeonggi Province, and Incheon City) is one of the most densely populated areas worldwide, with a population of approximately 20 million in 2016. Busan is the second-largest city in South Korea, with a population of approximately 3.4 million in 2016. Anmyeon is located southwest of Seoul, with petrochemical complexes, steel mills, and thermal power stations in this area. The background color in Fig. 1 represents the average NO_2 VCD obtained from the OMI during the KORUS-AQ campaign period, showing over 1×10^{16} molecules cm^{-2} over the Seoul metropolitan area. The OMI data were obtained with the Level 2.0 OMNO2 version 3.0 and downloaded from the NASA Earthdata search (http://search.earthdata.nasa.gov/search/). We calculated the arithmetic means of tropospheric NO_2 VCDs, like Choo et al. (2020), to obtain the grid data (0.25° × 0.25°) during the KORUS-AQ period. The average tropospheric NO_2 VCD data were excluded from May 30 2016 to Jun 9 2016, when the OMI data did not exist during the campaign period.

2.2 Pandora

NO_2 VCDs retrieved from the GeoTASO were validated using those from NASA's Pandora Spectrometer system. The Pandora spectrometer is a hyper-spectrometer that can provide direct sun measurements of UV-Vis spectra (280–525 nm with a full width at half maximum (FWHM) of 0.6 nm) for observing atmospheric trace gases. During the KORUS-AQ, eight Pandora instruments monitored NO_2 and ozone (O_3) VCD as depicted by plus symbols in Fig. 1. The retrieved data are available on the KORUS-AQ pages of NASA's Goddard Space Flight Center website (https://avdc.gsfc.nasa.gov/pub/DSCOVR/Pandora/DATA/KORUS-AQ/). We compared NO_2 VCDs obtained from five Pandora measurements (Busan university: 35.24 °N, 129.08 °E; Olympic park: 37.52 °N, 127.13 °E: Songchon: 37.41 °N, 127.56 °E; Yeoju: 37.34 °N, 127.49 °E; Yonsei University: 37.56 °N, 126.93 °E) within 0.05° and 30 min with those from GeoTASO. Because NO_2 has a short atmospheric lifetime, especially during the summer (Shah et al., 2020), its spatial and temporal distributions vary notably. A detailed description of Pandora's operation during the KORUS-AQ campaign has previously been reported (Herman et al., 2018; Spinei et al., 2018).

2.3 Ground-based in situ NO_2 measurement

Although the basic physical quantity of VCD and the surface mixing ratio from in situ measurements are different, comparison of their spatiotemporal variations provides useful information for deriving surface air quality from airborne instruments (e.g., Jeong and Hong, 2021a; 2021b). In this study, we compare the NO_2 VCDs (molecules cm^{-2}) retrieved from GeoTASO to surface mixing ratios measured by ground-based in-situ monitoring network over South Korea (i.e., Air-Korea, a national real-time air quality network; https://www.airkorea.or.kr/). The instruments use the chemiluminescence method (Kley and McFarland, 1980), and approximately 400 air quality monitoring sites in Korea are registered in the system, providing hourly surface NO_2 concentrations. We compared NO_2 VCDs retrieved from GeoTASO within 0.5 km and 30 min with NO_2 concentrations obtained from Air-Korea.

2.4 GeoTASO measurements

NO_2 VCDs were retrieved from the L1B radiance dataset (version: V02y) obtained using GeoTASO during the KORUS-AQ campaign. The NASA Goddard Space Flight Center conducted the L1B radiance calibration, which included offset and smear correction, gain matching, amplifier cross-talk correction, dark rate correction, integration normalization, sensitivity derivation, wavelength registration, geo-registration, non-linearity correction, and ground pixel geolocation (Kowalewski et al., 2017; Chong et al., 2020). The detailed specifications of GeoTASO are listed in Table 2 (Nowlan et al., 2016).

Table 2. Summary of the GeoTASO instrument and optical specification.

L1B version	V02y
Full cross-track field of view	45°
Single-pixel cross-track field of view	0.046°
Wavelength	UV: 290–400 nm VIS: 415–695 nm
Spectral resolution (full width at half maximum, FWHM)	UV: ~0.39 nm VIS: ~0.88 nm
CCD	1,056 (wavelength) × 1,033 (cross-track)
Spatial resolution before binning	~35 m (along-track) × 7 m (cross-track)
Spatial resolution after binning	~250 m (along-track) × 250 m (cross-track)

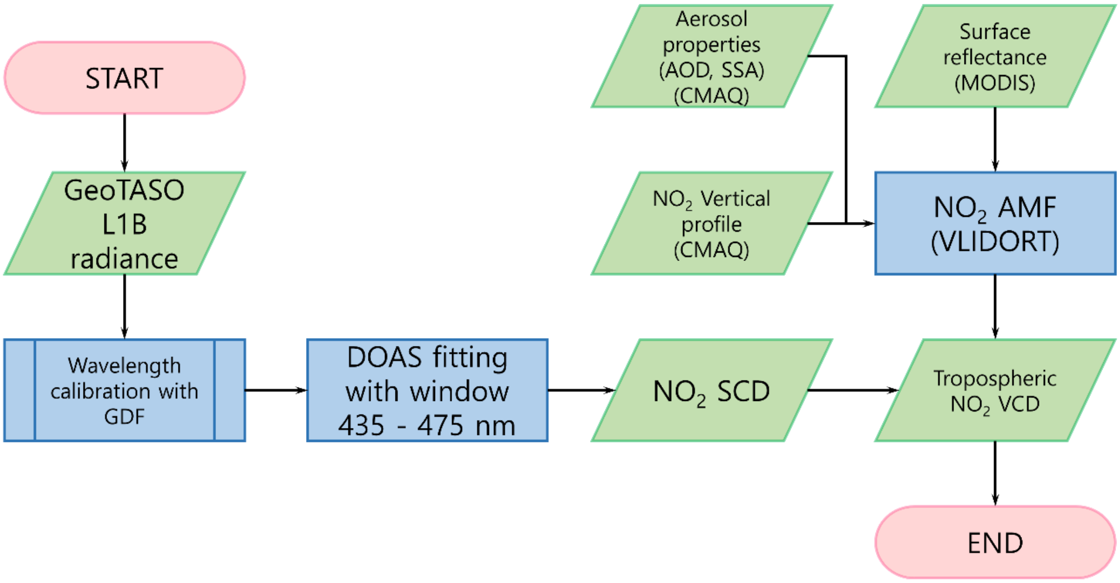

Figure 2. Flowchart of the algorithm for retrieving tropospheric NO_2 data from GeoTASO.

2.4.1 NO_2 slant column density retrieval

Figure 2 indicates the flowchart for retrieving the tropospheric NO_2 VCD from the GeoTASO. We first retrieved NO_2 SCDs using the DOAS method (Platt, 1994). Nonlinear least square minimization was used to retrieve the NO_2 SCDs which minimizes the difference between the measured optical depth and the modeled value in QDOAS software (Eq. (1); Danckaert et al., 2012).

$$\frac{\ln I(\lambda)}{\ln I_0(\lambda)} = -\left(\sum_{j=1}^{m} \rho_j \times \sigma'_j(\lambda) + B(\lambda) + R(\lambda) + A(\lambda) + N(\lambda)\right), \quad (1)$$

Where I(λ) is the measured earthshine radiance at wavelength λ; I_0 is the reference radiance from the reference sector (southern ocean of the Jeju Island denoted as the red circle in Fig. 1; 32.983°N, 126.392°E) at 9 AM on May 1 2016. The Community Multiscale Air Quality (CMAQ) modeling system data indicated that the NO_2 VCD from the surface to 50 hPa over this reference sector on this day was 6.75×10^{15} molecules cm-^{2}, and the mean of total NO_2 VCD obtained from the OMI during the KOURS-AQ period was 4.77×10^{15} molecules cm^{-2} with a standard deviation of 1.33×10^{15} molecules cm^{-2}. We also confirmed the stability of NO_2 distribution over this area using the TROPOMI offline data from 2019 to 2020. In this period, the NO_2 VCD from the TROPOMI was 4.81×10^{15} molecules cm^{-2} with a standard deviation of 0.43×10^{15} molecules cm^{-2}. The NO_2 VCD used as a reference sector obtained from CMAQ was mainly dominated by stratospheric NO_2 VCD. However, stratospheric NO_2 VCD has a relatively lower than tropospheric NO_2 VCD. The ρ_j represents the SCD of each species j; $\sigma'_j(\lambda)$ represents the differential gas phase absorption cross-section convolved with the Gaussian distribution function (GDF) with GeoTASO FWHM (the UV and VIS range were 0.34−0.49 nm and 0.70−1.00 nm, respectively (Nowlan et al., 2016)) at wavelength λ of species j, respectively.

We used the measured radiances at the reference sector to calculate differential slant column density (dSCD) over the whole domain of the GetoTASO measurements. CMAQ calculation over the reference sector (i.e., 6.75×10^{15} molecules cm^{-2}) was adopted as the reference SCD (SC_0), which is added to all dSCD values to convert to the SCD. The reference sector is known as a background area but is occasionally affected by the long-range transport of NO_2 from upwind areas. Considering the standard deviation of the OMI measurements accounts for such effects during the measurement period, we estimate the maximum uncertainties of the SC_0 can be calculated from this value (i.e., 1.33×10^{15} molecules cm^{-2}) in addition to the difference of the mean values between the CMAQ and OMI (i.e., 1.98×10^{15} molecules cm^{-2}). Therefore, our best estimate of the uncertainty of the SC_0 is the root of the sum of squares of these values (i.e., 2.38×10^{15} molecules cm^{-2}).

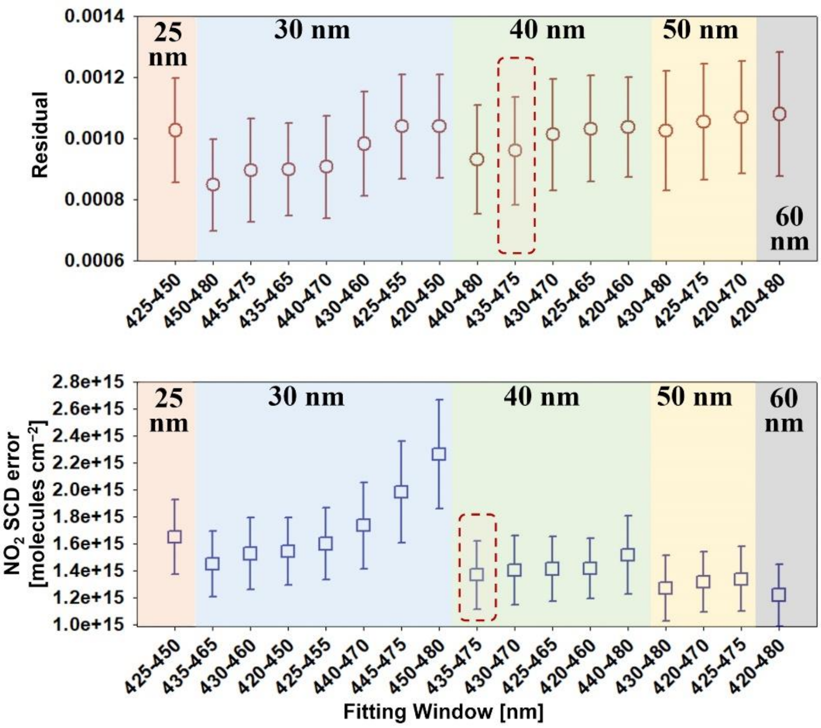

Figure 3. Residuals and NO_2 SCD errors of 17 spectral fitting window candidates (May 17, 2016, across track number: 15).

The spectral fitting window was selected based on the sensitivity test with 17 fitting window candidates from 420 to 480 nm with the length of the fitting window from 25 to 60 nm. Spectral fitting residuals and NO_2 SCD errors have been investigated for 17 spectral fitting window candidates (Fig. 3).

In terms of the residual, when the NO_2 fitting window includes a wavelength region less than 430 nm, it has a larger residual compared to the case where it does not. The higher residual can include the more noise signals that cannot be calculated mathematically, which can become an uncertainty for the NO_2 SCD retrievals. Therefore, we excluded the fitting window which includes wavelengths less than 430 nm for the GeoTASO NO_2 retrievals during the KORUS-AQ campaign. In the case of the NO_2 SCD error, it was confirmed that the longer the fitting window length, the lower the NO_2 SCD error appeared regardless of including the wavelength region less than 430 nm. Therefore, for the stable NO_2 SCD retrieval, an appropriate spectral fitting window needs to be selected which can minimize the residual with a moderate length of the fitting window. To find the optimal fitting window, we set the threshold value based on the above results: residual < 0.001, NO_2 SCD error < 1.4 $\times 10^{15}$ molecules cm^{-2}, the length of fitting window > 30 nm. Then, the fitting window of 435–475 nm was selected for the GeoTASO NO_2 retrievals during the KORUS-AQ campaign. To determine the wavelength registration more accurately in the narrow fitting window, additional wavelength calibration of the spectra for each of the 33 across track pixels was performed using a high-resolution solar reference spectrum (Kurucz solar spectrum) (Chance and Kurucz, 2010) with the GDF. The absorption cross-sections of NO_2 (Vandaele et al., 1998), O_3 (Bogumil et al., 2000), H_2O (Rothman et al., 2010), and the Ring effect as pseudo-absorbers (Chance and Spurr, 1997) were used to construct the model equation; and B(λ), R(λ), A(λ), and N(λ) are the broad absorption of trace gases, extinction by Mie and Rayleigh scattering, variation in the spectral sensitivity of the detector or spectrograph, and noise, respectively, which were accounted for by an 8th order polynomial. An example of the spectral fitting results is presented in Fig. 4.

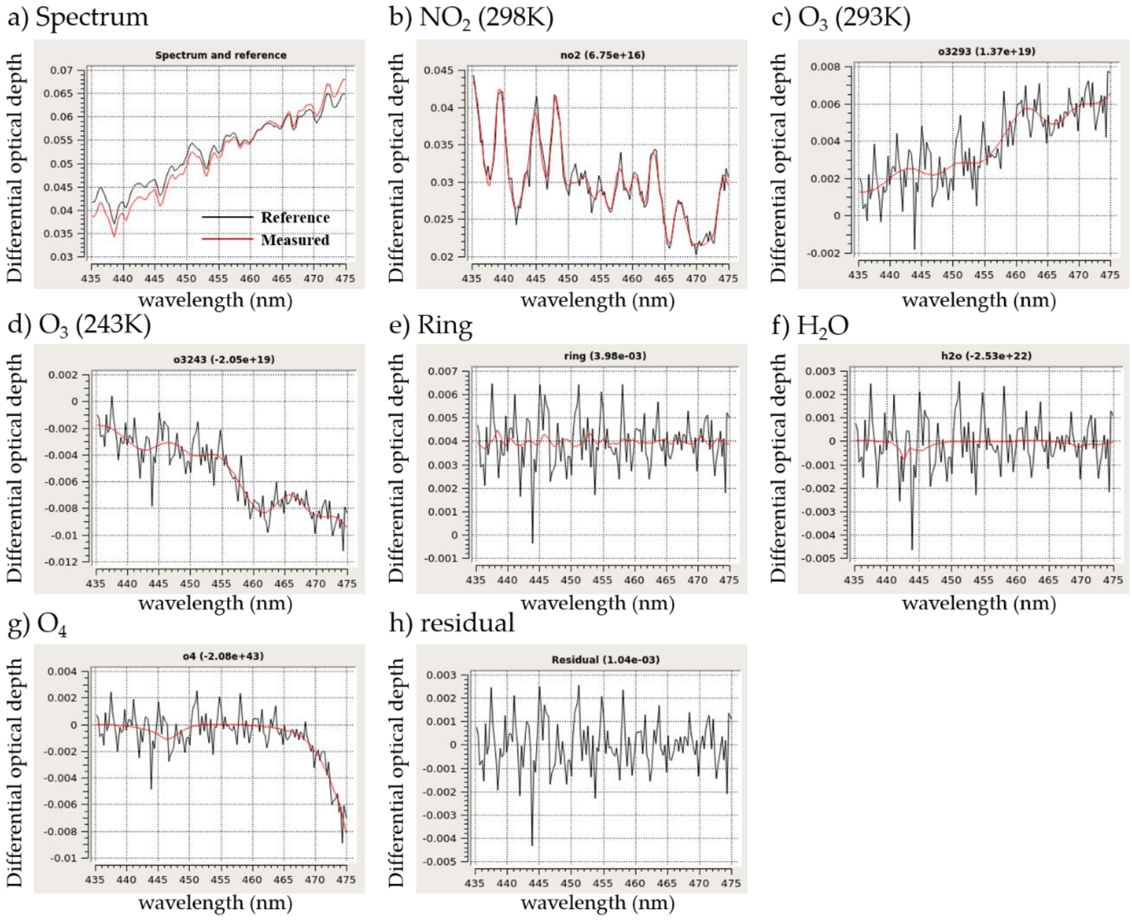

Figure 4. An example of the spectral fitting results of NO_2 retrievals from GeoTASO during the KORUS-AQ campaign (at Gangnam, Seoul on June 9, 2016). Red and black line in the panel (a) represent measured and reference spectrum, respectively. The panels of (b) to (h) depict examples of spectral fitting results of (b) NO_2, (c) O_3 (293 K), (d) O_3 (243 K), (e) ring, (f) H_2O, (g) O_4, where red and black lines are the absorption cross section of target species and the fitting residual plus the absorption of the target species, respectively. The panel (h) indicates the fitting residual of this example.

2.4.2 NO_2 AMF calculation

AMF, the ratio of SCD to VCD, can be calculated using the scattering weight (ω) and shape factor (S) (Palmer et al., 2001) in Eq. (2)−(5).

$$AMF = \frac{SCD}{VCD}, \tag{2}$$

$$AMF = AMF_G \int_{z1}^{z2} \omega(z) S(z) dz, \tag{3}$$

$$\omega(z) = -\frac{1}{AMF_G}\frac{\partial \ln I_B}{\partial \tau}, \tag{4}$$

$$S(z) = \frac{\alpha(z)n(z)}{\int_{z1}^{z2} \alpha(z)n(z)dz}, \tag{5}$$

Where AMF_G represents the geometric AMF, I_B is the earthshine radiance, τ is the optical depth, α is the absorption cross-section, and n is the number density of the absorber. NO_2 AMF was calculated using a linearized pseudo-spherical scalar and vector discrete ordinate radiative transfer model (VLIDORT, version 2.6; Spurr and Christi, 2014). Aerosol properties, such as AOD, SSA, APH, and *a priori* NO_2 vertical profile information, were simulated using the CMAQ, and surface reflectivity was obtained from MODIS (Collection 6). The surface reflectance products, MCD43A3, available at a 500 m spatial resolution, provide an estimate of the surface spectral reflectance including MODIS bands 1 through 7. Here, MODIS band 3 (459–479 nm) was used, because this band is the closest the wavelength (455 nm) used in the calculation of AMF in this study. APH was assumed to be the peak height of the aerosol extinction coefficient simulated in CMAQ, and the aerosol profile applied GDF based on APH (Hong et al., 2017). For pixels without reflectance information, AMF was not calculated. The products were corrected for atmospheric conditions, such as aerosol, gases, and Rayleigh scattering. In previous studies (Lamsal et al., 2017; Nowlan et al., 2018; Judd et al., 2019; Chong et al., 2020), an AMF was described for both above and below aircraft altitude is used to convert NO_2 SCDs to VCDs using Eq. (6)−(8).

$$AMF\uparrow = AMF_G \int_{Z_A}^{Z_{TOA}} \omega(z) S(z) dz, \tag{6}$$

$$AMF\downarrow = AMF_G \int_{Z_0}^{Z_A} \omega(z) S(z) dz, \tag{7}$$

$$NO_2\, VCD\downarrow = \frac{NO_2\, SCD - AMF\uparrow \cdot NO_2 VCD\uparrow}{AMF\downarrow}, \tag{8}$$

Where $AMF\uparrow$ and $AMF\downarrow$ are AMF above and below aircraft, respectively, and $NO_2\ VCD\uparrow$ represents NO_2 VCD above the aircraft obtained from a chemical transport model (CTM). However, here we calculated NO_2 VCD↓ by dividing NO_2 SCDs by $AMF\downarrow$ as the CMAQ only simulates the troposphere (surface to 50 hPa). However, as the stratospheric and free tropospheric NO_2 ($NO_2\ VCD\uparrow$) column densities over megacities and industrial areas are much lower than tropospheric NO_2 column densities, (Valks et al., 2011), we assume that the uncertainties in the *AMF* without considering the upper atmosphere are negligible in this study.

2.5 Chemical model description

Vertical profiles from CMAQ (Byun and Ching, 1999; Byun and Schere, 2006), a CTM, were used to calculate AMFs. The CMAQ simulations were conducted with a horizontal resolution of 15 × 15 km and had 27 vertical layers from the surface to 50 hPa. The meteorological fields were prepared using the advanced research Weather Research and Forecasting (WRF) Advanced Research WRF (ARW) Model (Skamarock et al., 2008). Anthropogenic emissions were generated based on the KORUS v5.0 model (Woo et al., 2012), and biogenic emissions were simulated using the Model of Emissions of Gases and Aerosols from Nature (MEGAN v2.1; Guenther et al., 2006; 2012). Besides anthropogenic and biogenic emissions, the Fire Inventory from NCAR (FINN; Wiedinmyer et al., 2006, 2011) was used to update the pyrogenic emission fields.

The CMAQ AOD was calculated by integrating the aerosol extinction coefficient (Q_{ext}), which is the sum of scattering (Q_{sca}) and absorption (Q_{abs}) coefficients, over all vertical layers (z) as follows:

$$AOD = \int Q_{ext}(z)\,dz \; = \int \{Q_{sca}(z) + Q_{abs}(z)\}\,dz, \tag{9}$$

$$Q_{abs}[Mm^{-1}] = \sum_i \sum_j \{(1-\omega_{ij}) \cdot \beta_{ij} \cdot f_{ij}(RH) \cdot [C]_{ij}\}, \tag{10}$$

$$Q_{sca}[Mm^{-1}] = \sum_i \sum_j \{\omega_{ij} \cdot \beta_{ij} \cdot f_{ij}(RH) \cdot [C]_{ij}\}, \tag{11}$$

Here, ω_{ij} indicates SSA of particulate species i for the particulate mode (or size bin) j, β_{ij} denotes the mass extinction efficiency, $f_{ij}(RH)$ is the hygroscopicity factor according to the relative humidity (RH), and $[C]_{ij}$ is the concentration of particulate species. CMAQ SSA is defined as the ratio of the integrated Q_{sca} to AOD, and NO_2 vertical profiles were obtained from NO_2 concentrations at each vertical layers by conducting CMAQ simulations. Details of the model descriptions and calculations of optical properties are given by Lee et al. (2020) and Malm and Hand (2007).

3 Results and discussion

3.1 NO_2 VCD retrieval

3.1.1 Seoul metropolitan region

We show the final NO_2 VCDs from 250 m spatial resolution. Because of NO_2 VCD, we selected the dates observed in both the morning and afternoon during the KORUS-AQ period over the Seoul metropolitan area, Busan, and Anmyeon. The retrieved dates for NO_2 VCDs were Jun 5, 9, and 10, 2016.

The population of the Seoul metropolitan region is approximately 20 million, which is approximately 40% of the total population of South Korea. It is rare to obtain high-resolution horizontal NO_2 VCD distributions using airborne measurements in the morning and afternoon, especially in Asian megacities. Figure 5 indicates tropospheric NO_2 VCDs over Seoul on June 9 2016, at 9 AM and 3 PM local time (LT). Because of an issue with imaging systems, enlarged views (Fig. 5-Fig. 8) present a slightly stripy appearance from the GeoTASO observation (Nowlan et al., 2016; Chong et al., 2020).

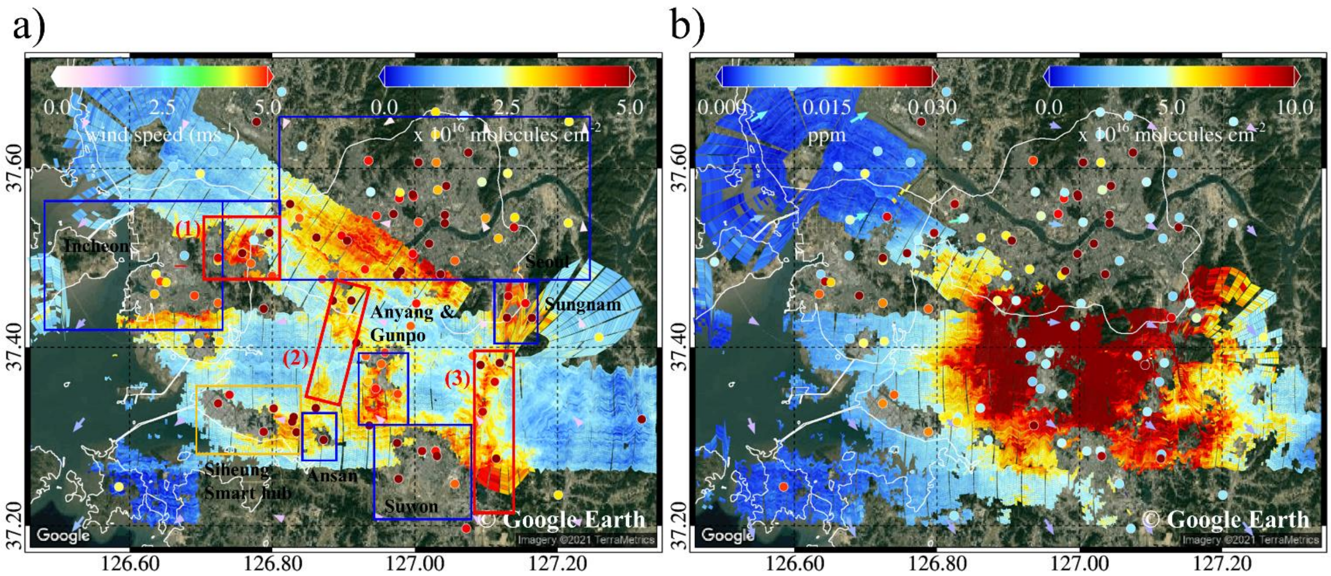

Figure 5. Tropospheric NO_2 VCD, in the Seoul metropolitan region onJune 9, 2016, retrieved from GeoTASO: a) at 9 AM and b) at 3 PM. The red boxes represent expressways (counterclockwise from left to right, (1) Gyeongin Expressway, (2) Seohaean Expressway, and (3) Gyeongbu Expressway), the orange box indicates the industrial complex, and the blue boxes indicate the major cities (Seoul, Incheon, Suwon, Bucheon, Anyang, Gunpo, Sungnam, and Ansan) of the Seoul metropolitan region. Colors of the circles depict the NO_2 surface mixing ratio obtained from Air-Korea. The color arrows indicate the wind direction and speed at 1000 hPa over Seoul metropolitan region, obtained via the Unified Model (UM) simulations (background RGB image is from Google Earth; https://www.google.com/maps/).

In the morning, NO_2 VCDs retrieved from GeoTASO were highly correlated with expressways (red boxes in Fig. 5), such as the Gyeongin, Seohaean, and Gyeongbu Expressways, and over major cities with heavy traffic, such as Seoul, Bucheon, Ansan, Anyang, and Suwon. GeoTASO observed NO_2 VCD values three-times higher (>3 × 10^{16} molecules cm^{-2}) in these areas compared to the surrounding rural areas. High NO_2 VCD values above 6 × 10^{16} molecules cm^{-2} were observed above the Gyeongin Expressway, which has very heavy traffic in a relatively short section, and the Gunpo Complex Logistics zone, where diesel vehicle traffic is also high. The main NO_2 source regions and the regions where high NO_2 VCD values were observed were highly consistent at 9 AM because the wind speed at this time—as obtained from the unified model (UM) based Regional Data Assimilation and Prediction System (RDAPS) of the Korea Meteorological Administration (KMA)—was as low as 0.1 ms^{-1} and the average wind direction was 84.7° at 1000 hPa over Seoul metropolitan region. The average daily traffic volume of these expressways exceeds 150,000 vehicles, and the total number of vehicles registered in these major cities is > 6,000,000, with an average daily mileage per car per day of over 38 km. Detailed information on these cities and expressways is listed in Table 3 and 4. Based on the level of vehicular traffic, combustion using gasoline and diesel engines leads to high overall emissions of NO_2 in the Seoul metropolitan region (Kendrick et al., 2015).

Table 3. The population, number of registered vehicles, and average mileage per car per day of the major cities in the Seoul and Busan metropolitan region obtained from the Korean Statistical Information Service (https://kosis.kr/eng).

City	Population (millions)	Vehicle registration number (thousands)	Average mileage (km car^{-1} day^{-1})
Seoul	9.776	3,083	37.1
Incheon	2.914	1,402	41.7
Bucheon	0.848	284	37.2
Ansan	0.744	289	40.8
Anyang	0.596	206	39.6
Gunpo	0.286	87	38.8
Suwon	1.241	467	38.1
Sungnam	0.994	358	36.3
Busan	3.389	1,295	40.1
Daegu	2.450	1,121	37.1
Changwon	1.080	551	37.5
Kimhae	0.529	250	38.0

Table 4. Daily average traffic volume on the Gyeongin, Gyeongbu, and Seohaean Expressways obtained using the Traffic Monitoring System (https://www.road.re.kr).

Expressway	Daily average traffic volume
Gyeongin Expressway	162,369
Gyeongbu Expressway	173,413
Seohaean Expressway	150,298

Compared to the data of the morning, the average wind speed and wind direction were 1.7 ms^{-1} and 284.5° at 1000 hPa in the afternoon and the afternoon had extremely high tropospheric NO_2 VCD values (exceeding 5×10^{16} molecules cm^{-2}) in most of the Seoul metropolitan regions including rural areas, whereas the NO_2 mixing ratio (MR) obtained from Air-Korea decreases in the afternoon. According to Tzortziou et al. (2018), similar results were retrieved from the Pandora site in Seoul, with higher afternoon NO_2 VCDs than in the morning. This result is because the amount of NO_2 produced by chemical conversion of nitric oxide (NO) by O_3 and VOCs in the atmosphere, along with NOx generated by regional emissions (traffic) in the Seoul metropolitan region, is greater than the amount lost by photolysis and transport to nearby areas (Herman et al., 2018). Furthermore, the increase in tropospheric NO_2 VCD in the afternoon is likely due to the accumulation and dispersion of NO_2 according to the height of the change in the planetary boundary layer (Ma et al., 2013).

3.1.2 Industrial and power plant regions in Anmyeon

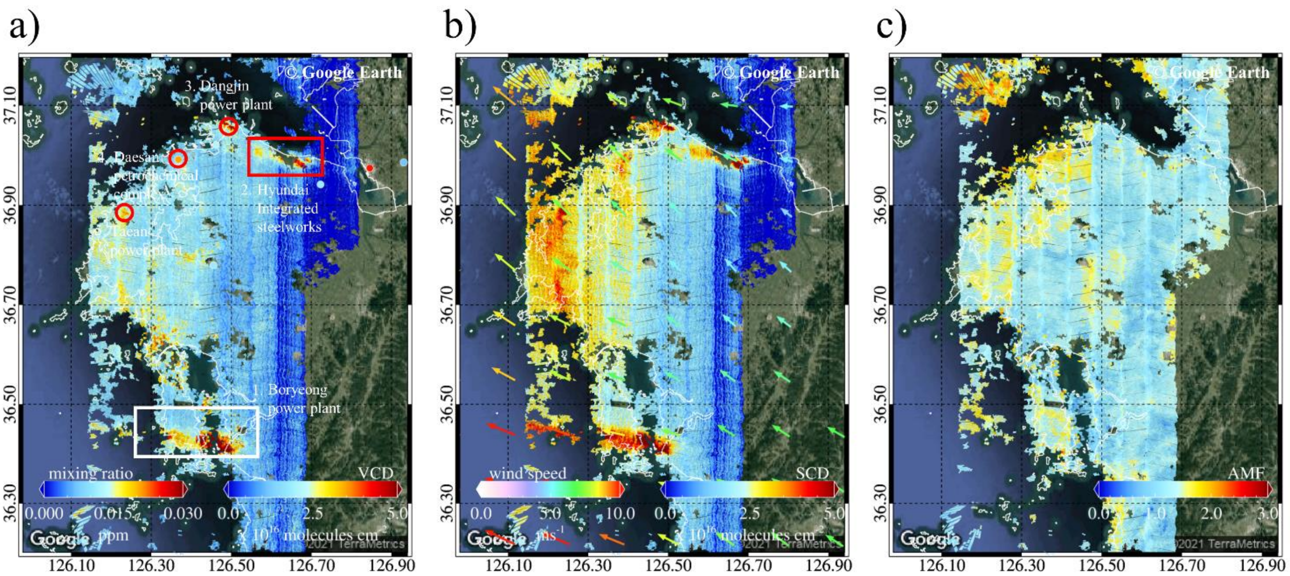

Figure 6. a) Tropospheric NO_2 VCD and b) NO_2 SCD retrieved from GeoTASO, and c) NO_2 AMF, native resolution (250 m) calculated using VLIDORT over Anmyeon in South Korea on 5 June 2016. The colored arrows indicate wind speed and wind direction at 850 hPa from the Unified Model (UM) simulations. The red circles and rectangle in panel (a) represent the major NO_2 emission sources, such as steelworks and power plants (background RGB image is from Google Earth; https://www.google.com/maps/).

The high spatial resolution of the tropospheric NO_2 VCD from GeoTASO over the Anmyeon industrial region, where many industrial facilities and several power plants are distributed, is shown in Fig. 6. Panels a and b of this figure indicate the binned tropospheric NO_2 VCD and NO_2 SCD retrieved from GeoTASO L1B data, respectively, between 13:00 and 17:00 LT on June 5 2016. Panel c depicts the calculated AMF of NO_2 from native resolution over the domain. GeoTASO observations detected moderate and strong NO_2 emission sources in this area: (1) Boryeong power plant, (2) Hyundai integrated steelworks, (3) Dangjin power plant, (4) Daesan Petrochemical Complex, and (5) Taean Power Plant. High NO_2 VCD values (> 5×10^{16} molecules cm^{-2}) were observed over steel mill works, petrochemical complexes, and power plants, whereas values were comparatively low (<1×10^{16} molecules cm^{-2}) over small cities including Seosan, Dangjin, and Boryeong with populations of less than 0.1 million, and the Seohaean Expressway. In 2016, the annual NOx emissions from Hyundai steelworks and the Dangjin and Boryeong power plants were approximately 10.3, 11.9, and 16.8 kt $year^{-1}$, respectively. The NOx emission rates of major industrial facilities in the Anmyeon region are shown in Table 5.

Table 5. NOx emission rates in 2016 from major industrial facilities in the Anmyeon region obtained from the Continuous Emission Monitoring System of the Korea Environment Corporation (https://www.stacknsky.or.kr/eng/index.html).

Industrial facilities	NOx emission rate (kg $year^{-1}$)
Boryeong power plant	16,788,438
Hyundai integrated steelworks	10,271,075
Dangjin power plant	11,852,972
Daesan petrochemical complex	3,397,939
Taean power plant	15,466,022

Figure 6 shows high NO_2 concentrations of the main industrial facilities in the Anmyeon region, where the combustion of fossil fuel in factories and thermal power plants leads to high emissions (Prasad et al., 2012). Due to relatively sparse distribution over rural areas, the Air-Korea measurements did not detect the major NO_2 plume as shown in Fig. 6a. Thus, airborne remote sensing systems, such as GeoTASO, can effectively complement ground-based networks for monitoring minor and major NOx emissions, particularly over these remote industrial regions.

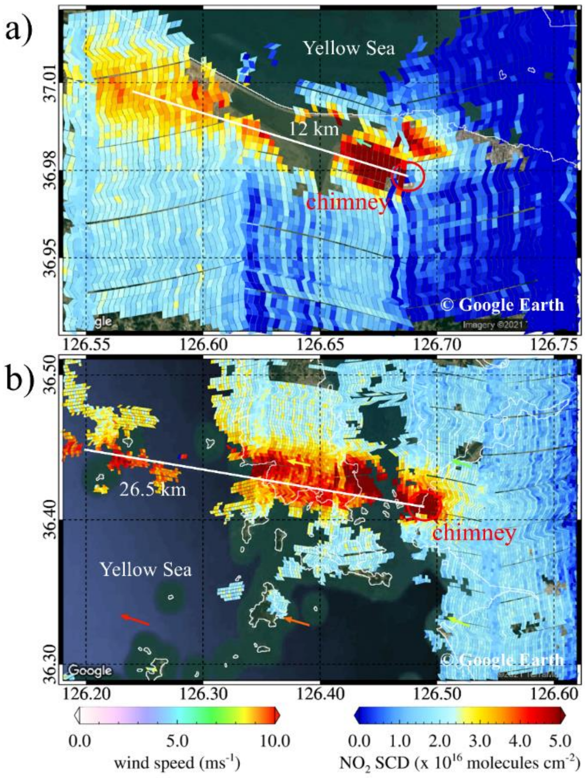

Figure 7. Enlarged view of GeoTASO tropospheric NO_2 SCD observation over a) Hyundai steel works, indicated by the red box in Figure 6, and b) the Boryeong power plant, indicated by the white box in Figure 6. The arrows represent the wind direction and speed at 850 hPa from the Unified Model (UM) simulations, respectively (background RGB image is from Google Earth; https://www.google.com/maps/).

The GeoTASO data captured not only NOx emissions from the chimneys of steelworks and power plants but also its transport by the wind. Figure 7a and 7b show enlarged views of tropospheric NO_2 SCD retrieved using GeoTASO over the Hyundai steelworks (red box in Fig. 6) and the Boryeong power plant (white box in Fig. 6). The arrows in Fig. 7 represent the prevailing wind direction and speed from RDAPS. NO_2 emitted from the chimneys of these sites was transported to the Yellow Sea, traveling distances of over 26.5 km at speeds of approximately 6 ms^{-1}. According to Chong et al. (2020), similar results were found for SO_2 emitted and transported from these sites.

3.1.3 Busan metropolitan region

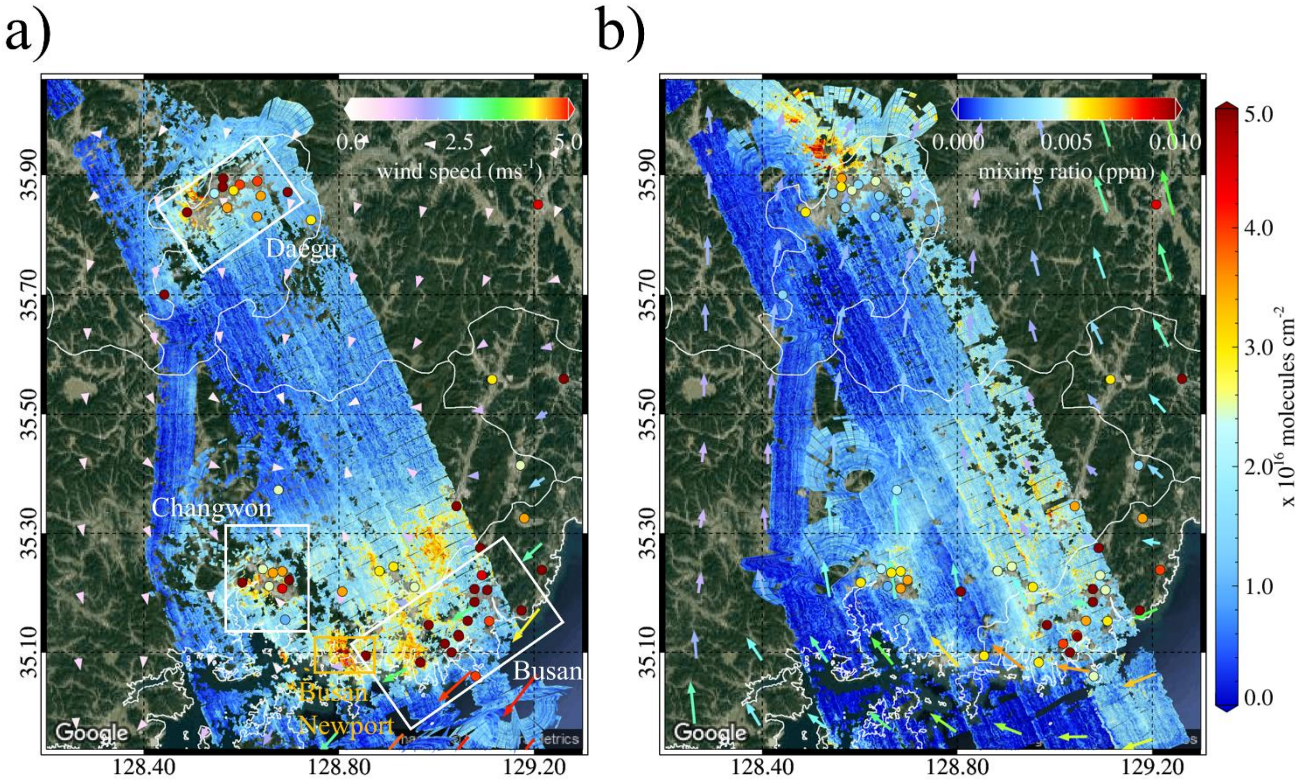

Figure 8. Tropospheric NO_2 VCD in the Busan metropolitan region in the (a) morning and (b) afternoon of June 10, 2016. The wind speed (colors scale) and wind direction (arrows) at 1000 hPa pressure level were obtained from the Unified Model (UM) simulations. The white boxes represent major cities such as Busan, Daegu, and Changwon. The orange box represents Busan Newport (the background RGB image is from Google Earth; https://www.google.com/maps/).

Figure 8a and 8b show tropospheric NO_2 VCD retrieved from the GeoTASO L1B data over the Busan metropolitan region on June 10 2016 in the morning (between 08:00 and 11:00 LT) and afternoon (between 13:00 and 16:00 LT), respectively. The arrows in Fig. 8 indicate the wind speed and wind direction of 1000 hPa obtained from the UM-RDAPS, with the average wind speed and wind direction of 0.9 ms^{-1}, and 55.4°, 1.9 ms^{-1} and 147.0°, respectively, in the morning and afternoon. High NO_2 VCDs were observed above urban areas, port, industrial complexes, and the inter-city road between Busan and Changwon. Like the Seoul metropolitan regions, combustion using gasoline and diesel engines is estimated to contribute to the high NOx emission. In the morning, NO_2 VCDs were high (approximately 3×10^{16} molecules cm^{-2}) in the major cities and, especially, around Busan Newport, with values exceeding 7×10^{16} molecules cm^{-2}. In comparison, in the mountainous regions between Daegu and Busan, the NO_2 VCD values were less than 1×10^{16} molecules cm^{-2} during the same period. The spatial distribution of tropospheric NO_2 VCDs was like that in the Seoul metropolitan regions, with high values over major cities and roads (compare Figs. 5 and 8). In Busan, fossil fuel combustion that uses both road vehicles and ships is likely to contribute to the NOx emissions. In the afternoon, unlike the Seoul metropolitan region, tropospheric NO_2 VCD over Busan decreased by over 3×10^{16} molecules cm^{-2}, which also corresponds with NO_2 MR data obtained from the Air-Korea sites. Detailed information on these cities is listed in Table 3.

3.2 Error estimation

The accuracy of the NO_2 VCD retrieval using the DOAS method depends on both the AMF calculation and the spectral fitting error of the SCD retrieval. Retrieval errors of the NO_2 VCD were estimated using error propagation analysis as expressed in Eq. (12).

$$\frac{\varepsilon_{VCD}}{VCD} = \sqrt{(\frac{\varepsilon_{SCD}}{SCD})^2 + (\frac{\varepsilon_{AMF}}{AMF})^2}, \qquad (12)$$

Where ε_{VCD} is the total error of NO_2 VCD. The error of NO_2 SCD (ε_{SCD}) is obtained from the spectral fitting error of NO_2 SCD via the DOAS spectral fitting. ε_{AMF} indicates the error of NO_2 AMF caused by uncertainties in the model input parameters for AMF calculation. Uncertainties in aerosol properties (AOD, SSA, and APH) and surface reflectance for the RTM calculations are the major factors affecting NO_2 AMF accuracy (Boersma et al., 2004; Leitão et al., 2010; Hong et al., 2017). Therefore, in this present study, we quantified the NO_2 AMF errors (ε_{AMF}) due to uncertainties in the input parameters independent of each other using Eq. (13):

$$\varepsilon_{AMF} = \sqrt{(\frac{\partial AMF}{\partial AOD})^2 \sigma AOD^2 + (\frac{\partial AMF}{\partial SSA})^2 \sigma SSA^2 + (\frac{\partial AMF}{\partial ALH})^2 \sigma ALH^2 + (\frac{\partial AMF}{\partial SFR})^2 \sigma SFR^2} = \sqrt{\sum_{i=1}^{4} (\frac{\partial AMF}{\partial \chi_i})^2 \sigma_{\chi_i}^2}, \qquad (13)$$

where $\frac{\partial AMF}{\partial \chi_i}$ are partial derivatives of NO_2 AMF regarding the input parameters (χ_i), $\sigma_{\chi i}$ represents the uncertainty of the χ_i. The σ of AOD, SSA, surface reflectance, and APH are assumed to be 30% (Ahn et al., 2014), 0.04 (Jethva et al., 2014), 0.005 + 0.05 × surface reflectance (EOS Land Validation; https://landval.gsfc.nasa.gov), and 1 km (Fishman et al., 2012), respectively, in this study. To derive $(\frac{\partial AMF}{\partial \chi_i})^2$, the true χ_i is input to the RTM to simulate 'true' NO_2 AMF. For the AOD, SSA, APH, and surface reflectance (SFR), perturbed NO_2 AMF was simulated using RTM with $\chi_i \pm \sigma\chi_i$. $\partial\chi_i$ denotes the difference between the 'centre' χ_i and $\chi_i \pm \sigma\chi_i$, and ∂AMF is the difference between the 'centre' NO_2 AMF (AMF_{centre}) simulated with 'centre' input values and the perturbed NO_2 AMF ($AMF_{perturbed}$) simulated using the perturbed input parameters $\chi_i \pm \sigma\chi_i$ (i.e. the original input parameters modified by the uncertainty). The simulation for calculating the ε_{AMF} was conducted using the input parameters on 9 June 2016.

Table 6. Total NO_2 VCD caused by uncertainties in NO_2 SCD and NO_2 AMF (the average for the flight on June 9, 2016).

NO_2 AMF errors	AOD	2.8%
	SSA	4.1%
	Aerosol peak height	22.3%
	Surface reflectance	2.8%
	Total NO_2 AMF error due to aerosol uncertainties	**23.3%**
NO_2 SCD error		**11.7%**
NO_2 VCD error		**26.9%**

Table 6 lists the estimated NO_2 VCD error on June 9 2016 for each source based on the error propagation method. The error estimation was conducted for the pixels where root mean square residual < 0.001 and NO_2 VCD > 5×10^{15} molecules cm^{-2} since NO_2 SCD precision is reported to be highly decreased in low NO_2 conditions (Hong et al., 2017). The total NO_2 VCD error was 26.9% with a high portion of NO_2 AMF error. The NO_2 SCD error was calculated to be 11.7%, showing the importance of accurate DOAS spectral fitting for deriving NO_2 SCD. The total AMF error due to uncertainties in the input parameters was calculated to be 23.3%. Among model input parameters, the effect of APH on NO_2 AMF becomes high (22.3%), indicating the importance of accurate aerosol profile information. APH sensitively affects NO_2 AMF because near the surface where trace gases and aerosols are well mixed, aerosols lead to multiple scattering effects and the light absorption of trace gases is due to increasing light path (Castellanos et al., 2015; Hong et al., 2017). Especially, APH can be the most important input parameter in the Asia region where high loadings of aerosol plumes persist throughout the year. The NO_2 AMF calculation errors due to uncertainties in SSA and AOD were 4.1% and 2.8%, respectively. The NO_2 AMF calculation error due to uncertainties in aerosol optical properties (SSA and AOD) appears to be smaller than those in a previous study (Leitão et al., 2010). The smaller effect of the aerosol properties can be explained by the moderate aerosol loading (AOD = 0.40) on the day of flight day. The NO_2 AMF errors become larger under high AOD conditions. The smallest effect of SRF was found on NO_2 AMF calculation error, which was calculated based on the uncertainty of the SRF of the satellite-based product (MODIS). Therefore, it may be an unrealistic number for the airborne NO_2 AMF calculation. Once the uncertainty of airborne-based SRF is provided, considering its measurement geometry and finer spatial resolution, more realistic airborne-based NO_2 AMF calculation error due to uncertainties in SRF can be estimated. The can of the *a priori* NO_2 profile shape also be a factor to cause calculation error for NO_2 AMF, as reported in previous studies (Leitão et al., 2010, Meier et al., 2016, Hong et al., 2017). Therefore, it is necessary to calculate the contribution of the shape of the NO_2 profile *a priori* on the accuracy of NO_2 AMF in the future. Moreover, the resulting uncertainties of input parameters of a GeoTASO ground pixel need to be considered by combining the initial uncertainties of CTM and satellite-based products, and by the variability of the parameters within the respective CTM (AOD, SSA, and APH) and satellite (SFR) grid box. If values such as SFR are assumed constant over larger areas, the fundamental spatial variability in this these data increases the uncertainty of the AMF and hence of the determined NO_2 VCD on the respective finer spatial scale. In addition, the uncertainty from the assumption on the SC_0 and the uncertainty from ignoring the NO_2 above the aircraft in the AMF calculations are needed to be considered in the error analysis. This analysis should be considered in further study.

$$AMF_{percent\_change} = \frac{AMF_{perturbed} - AMF_{centre}}{AMF_{centre}} \times 100, \quad (14)$$

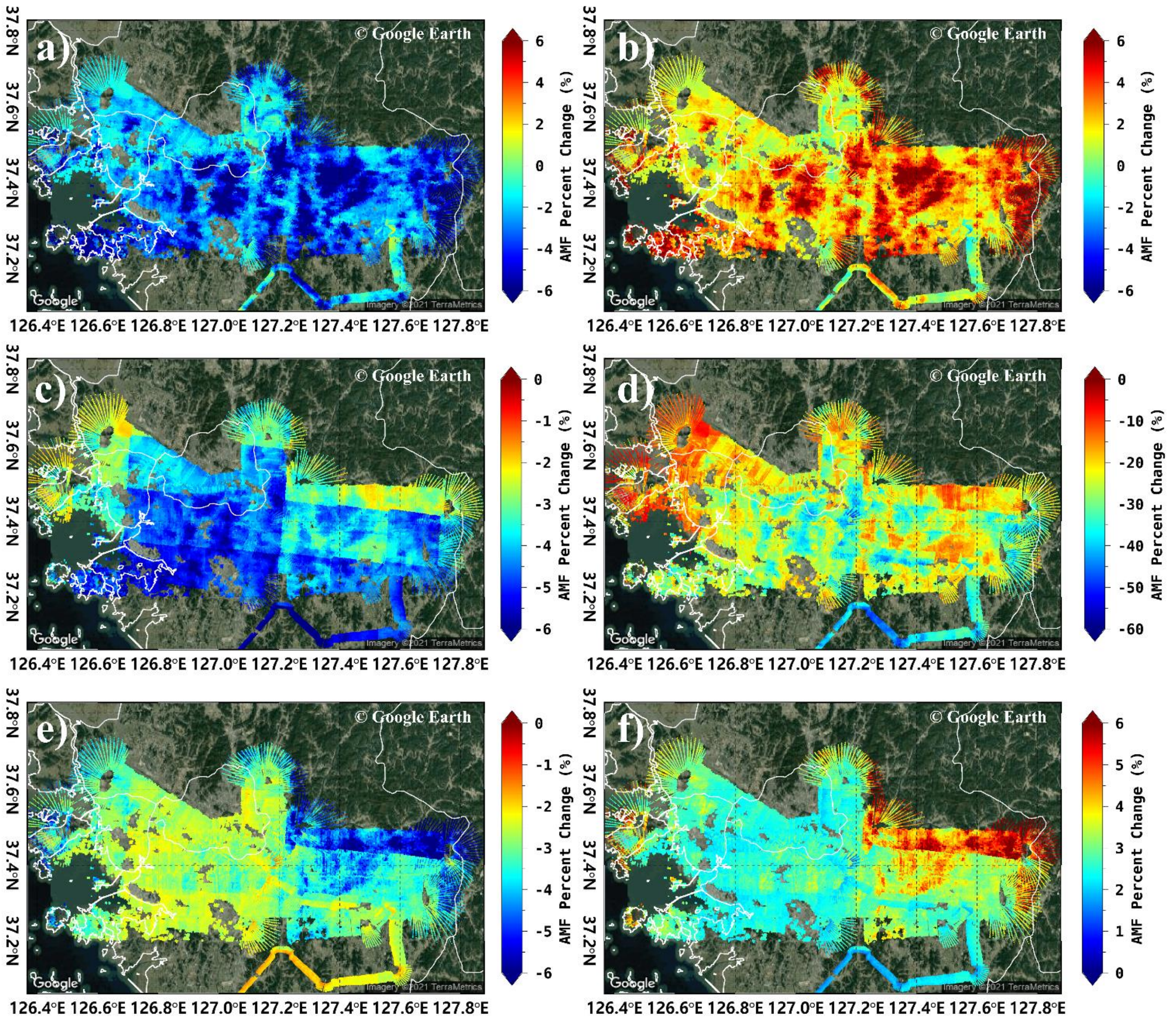

Figure 9. Percent change between AMF calculated using the CMAQ model simulation and those using a) 30% lower AOD, b) 30% higher AOD, c) 0.04 lower SSA, d) 1km higher APH, compared to the model outputs. The percentage change for AMF calculated using MODIS data and those using e) 0.005 + 0.05 × SFR lower SFR, f) 0.005 + 0.05 × SFR higher SFR (background RGB image is from Google Earth; https://www.google.com/maps/).

In this study, we also investigated the spatial distribution of AMF calculation errors associated with uncertainties in aerosol properties (AOD, SSA, and APH) and SFR. The percent change in NO_2 AMF ($AMF_{percent\_change}$) was calculated on each spatial pixel using Eq. (14). Figure 9a and 9b indicate the percentage change error between the calculated AMFs using the CMAQ AOD data with 30% lower (Fig. 9a) and 30% higher (Fig. 9b) values, respectively. The AMF decreased and increased by up to 10% with decreasing and increasing AOD, respectively, in the Seoul metropolitan region. We estimated that, under low aerosol loading conditions, an increase in AOD near the surface leads to an increase in the scattering probability within the surface layer with high NO_2 concentrations. Figure 9c indicates the percent change error between the calculated AMFs using CMAQ SSA data with a 0.04 lower value. The AMF decreased with decreasing SSA because the absorption of light increased. APH was also found to highly affect the accuracy of the AMF calculations (Fig. 9d). The APH uncertainty of 1 km decreased the AMFs with an average $AMF_{percent\_change}$ of -25% on the flight day. Especially, on the pixels where AOD > 0.6, the average $AMF_{percent\_change}$ was found to be -26% whereas that was -27% on the pixels where AOD < 0.4, showing the combined effect of aerosol loading and aerosol profile shape on the NO_2 AMF calculations. Figure 9e and 9f indicate the percentage change error between the calculated AMFs using the MODIS surface reflectance data with 0.005 + 0.05 × SFR lower (Fig. 9e) and 0.005 + 0.05 × SFR higher (Fig. 9f) values, respectively. The AMF decreased by approximately 3% when the SFR decreases, and vice versa when it increased.

3.3 Validation of NO_2 VCDs retrieved from GeoTASO

The tropospheric NO_2 VCDs retrieved from GeoTASO L1B data ($NO_{2,G}$) were compared with those obtained from OMI total NO_2 VCDs ($NO_{2,O}$) and Pandora ($NO_{2,P}$). The $NO_{2,O}$ were only available for June 10 during the campaign period. Therefore, we compared only 48 $NO_{2,G}$ and $NO_{2,O}$ data points within a radius of 20 km and 30 min, which yielded a correlation coefficient of 0.48 with a slope of 0.13 (Fig. 10 a). To validate, All $NO_{2,G}$ within a radius 20 km of the OMI center coordinate were averaged.

The NO_2 values are relatively low, as GeoTASO observation is conducted in a region with low NO_2 compared to the Seoul metropolitan and the overpass time of OMI is approximately 13:30 LT when NO_2 decreased. The low slope value is because the OMI with low spatial resolution does not reflect the spatial NO_2 inhomogeneity in the pixel.

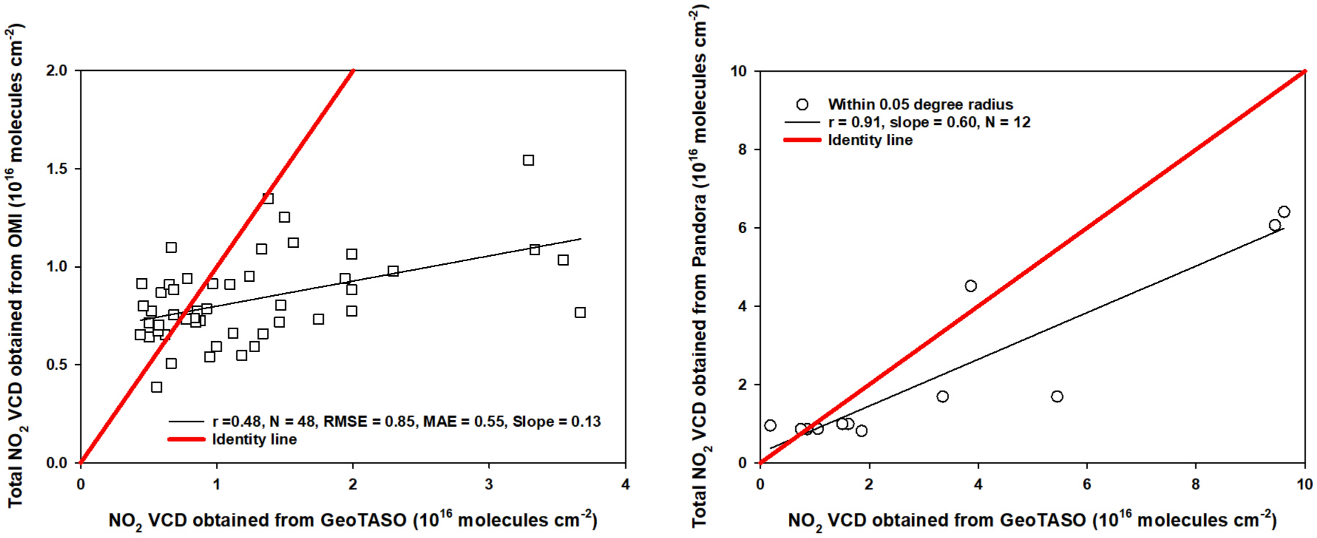

Figure 10. Scatter plots of a) NO_2 VCD retrieved from GeoTASO and total NO_2 VCD obtained from OMI and b) total NO_2 VCD obtained from Pandora and NO_2 VCD retrieved from GeoTASO, respectively.

To compare $NO_{2,G}$ data, we made a comparison with total NO_2 VCD obtained from the Pandora system ($NO_{2,P}$) during the KORUS-AQ campaign period. $NO_{2,P}$ obtained from Busan University, Olympic Park, Songchon, Yeoju, and Yonsei University Pandora sites on June 5, 9, and 10 were used for the GeoTASO validation (Fig. 1). $NO_{2,G}$ and $NO_{2,P}$ columns at these sites are compared in Fig. 11. To compare $NO_{2,G}$ and $NO_{2,P}$, we used averaged $NO_{2,G}$ retrieved from 16 across tracks with the smallest viewing zenith angle and averaged 30 min NO_2 obtained from pandora measurement within a radius of approximately 0.05°. $NO_{2,G}$ and $NO_{2,P}$ were correlated (R = 0. 91, with a slope of 0.60), however, when $NO_{2,P}$ was lower than 1×10^{16} molecules cm^{-2}, the correlation coefficient between $NO_{2,G}$ and $NO_{2,P}$ was < 0.1. The weak correlation at low NO_2 levels most likely reflects differences in viewing geometries and the horizontal inhomogeneity of the measured NO_2 between Pandora and GeoTASO. Furthermore, Pandora and GeoTASO can be used for the NO_2 validation of geostationary satellites, such as GEMS. However, because the number of pandora is limited in this campaign, we difficulty validating NO_2 retrieved from GeoTASO under various conditions. Many ground-based remote sensing measurements are needed to validate GEMS under various conditions.

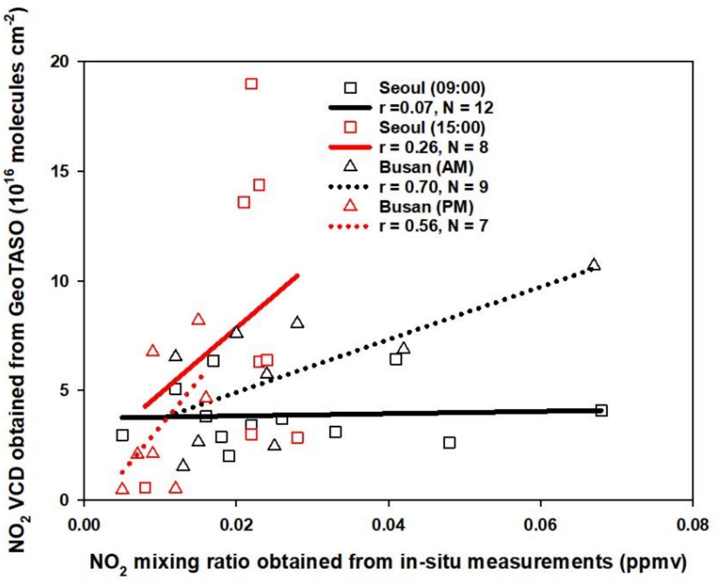

Figure 11. Scatter plot of the NO_2 VCDs retrieved from GeoTASO, and NO_2 surface mixing ratio obtained from Air-Korea. The black and red squares represent the NO_2 data at 9 AM and 3 PM (local time) in the Seoul metropolitan region, respectively. The black and red triangles represent those in the morning and afternoon, over Busan, respectively.

To compare the spatiotemporal distribution of NO_2 VCDs retrieved from GeoTASO, $NO_{2,G}$ compared with surface spatial patterns, $NO_{2,G}$ was compared with $NO_{2,A}$ for GeoTASO data within a radius of approximately 0.05 km and 30 min (Fig. 11). To compare $NO_{2,G}$ and $NO_{2,A}$, we used averaged $NO_{2,G}$ retrieved from 16 across tracks and averaged 30 min within a radius of 0.05°. Because in situ measurements provide NO_2 VMR ($NO_{2,A}$)(ppmv) once per hour, $NO_{2,A}$ of the nearest time is used to compare with $NO_{2,G}$.The correlation coefficient (R) between $NO_{2,G}$ (molecules cm^{-2}) and $NO_{2,A}$ at 9 AM and 3 PM LT in the Seoul metropolitan region was 0.07 and 0.26, respectively. When using only roadside station data from Air-Korea, the R-value for the morning increased to 0.72, which implies GeoTASO is more sensitive to emissions from NO_2 source areas, such as roadsides (Fig. 5). Because the comparison, there were large differences in the morning and afternoon. These results were identified because synoptic meteorology played an important role from June 1 to June 10, 2016 (Choi et al., 2019). As described by Judd et al. (2018), the spatial distribution for NO_2 VCDs appears to reflect the emission source in local industrialized regions and transportations in the morning with relatively weak winds. NO_2 concentration often increases in the late morning, indicating that the emission process proceeds faster than the NO_2 removal process. As the planetary boundary layer heights (PBLH) in early afternoon increase and surface NO_2 is mixed through a deeper PBLH, the NO_2 VCDs distribution showed a wider increase in most of the Seoul metropolitan area and the column amounts continue to increase (Judd et al., 2018).

When comparing NO_2 VCDs with surface NO_2 concentrations, it should be highlighted that it is a nonlinear relationship between $NO_{2,G}$ and $NO_{2,A}$. Although it may vary depending on weather conditions, high NO_2 VCDs from airborne observations can sometimes be detected with low surface NO_2 concentrations. When exhaust gases emitted from industrial facilities occur at a certain altitude (stacks/chimneys), $NO_{2,G}$ show high NO_2 VCDs, but $NO_{2,A}$ may be observed to have a low concentration. Unfortunately, in the Anmyeon industrial region, $NO_{2,G}$ and $NO_{2,A}$ could not be compared due to spatial restrictions because the distribution of ground observation stations is concentrated in metropolitan areas.

In the Busan metropolitan area, the R-value of the $NO_{2,G}$ and $NO_{2,A}$ data had a correlation coefficient greater than 0.56. This reflects the more even horizontal distribution of NO_2 in the afternoon, when diffusion from the source areas had occurred. However, for a more accurate comparison, NO_2 VCD data should be converted to NO_2 MR based on mixing layer height, temperature, and pressure profile data (Kim et al., 2017; Qin et al., 2017; Jeong and Hong, 2021a). However, because the number of pandora and satellite data is limited in this campaign, we had difficulties in validating NO_2 retrieved from GeoTASO under various conditions. Because ground-based, airborne and space borne remote sensing measurements have their own advantages and disadvantages, it is recommended a comprehensive observation campaign involving all of ground-based, airborne and space-borne measurements should be conducted continuously for the upcoming new era of geostationary environmental satellites.

4 Conclusions

For the first time, we have retrieved NO_2 VCD data using airborne GeoTASO observations over the Seoul metropolitan region—one of the most populous cities worldwide, the Busan metropolitan region—the second-largest city in South Korea, and Anmyeon, with thermal power plants and industrial complexes. By retrieving NO_2 data using GeoTASO L1B radiance, it was possible to observe the spatial distribution of NO_2 in these metropolitan and industrial regions. In the morning, tropospheric NO_2 VCD in Seoul showed a strong horizontal gradient between rural and urban areas. In urban areas, tropospheric NO_2 VCD was high, with values exceeding 3×10^{16} molecules cm^{-2}; in rural areas, values were typically below 1×10^{16} molecules cm^{-2}. Extremely high values over 10×10^{16} molecules cm^{-2} were also observed in both rural and urban areas. In Anmyeon, GeoTASO observations showed that NO_2 is mainly emitted from the chimneys of industrial complexes and thermal power plants, and subsequently transported by wind approximately 30 km to the Yellow Sea on the west coast of the Korean Peninsula. In the Busan metropolitan region, in the morning, tropospheric NO_2 VCDs showed a pattern similar to the Seoul metropolitan region, with high values above the inter-city road. However, unlike Seoul, tropospheric NO_2 VCDs in Busan decreased in the afternoon due to local different weather conditions locally.

To compare the data retrieved from the GeoTASO system, we compared $NO_{2,G}$ with $NO_{2,O}$ obtained from the OMI, $NO_{2,A}$ obtained from Air-Korea, and $NO_{2,P}$ obtained from the Pandora observation system. When the distance between two observations was below 20 km or 0.05° within 30 min, the correlation coefficients were relatively high ($R = 0.48$, and 0.91, respectively). However, the correlation between $NO_{2,G}$ and $NO_{2,A}$ over the Seoul metropolitan region was extremely weak ($R = 0.07$) in the morning because of the more pronounced NO_2 horizontal gradient.

The GeoTASO system successfully observed NO_2 VCDs with high horizontal spatial resolution for both metropolitan and industrial regions. This demonstrates that airborne remote sensing measurements from GeoTASO, similar to GCAS, APEX and others, can be an effective tool for the validation of trace gases retrieved from environmental satellites, including the OMI, TROPOMI, and GOME-2; these systems can obtain high-resolution measurements over relatively wide areas. However, to validate geostationary environmental satellites with higher spatiotemporal resolutions, such as the GEMS, TEMPO, and sentinel-4, additional validation strategies are needed. Based on error estimation, it can be concluded that aerosol properties are relevant and should be determined and NO_2 vertical profile retrieval performed using, for example, LIDAR, MAX-DOAS, and sondes. This is important because the accuracy of aerosol properties, surface reflectance and the NO_2 vertical profiles affects the accuracy of AMF calculations (Leitão et al., 2010; Hong et al., 2017; Lorente et al., 2017; Boersma et al., 2018). Furthermore, as we observed in the Seoul metropolitan area, closer spaced observations using ground-based remote sensing systems and in situ measurements are needed as NO_2 displays large horizontal gradients, especially in the morning.

Author contributions

GH and **HH** designed and implemented the research. **KL** provided the CTM data. **GH** developed the code for model running and performed the RTM simulations. **HH** and **UJ** contributed to the analysis of ground-based data. **GH** and **WC** conducted the sensitivity test. **GH**, **KL**, **HH**, **UJ**, **WC,** and **JJS** revised and edited the paper. **HH**, **UJ, and WC** provided constructive comments. All authors contributed to this works.

Competing interests

The authors declare that they have no conflict of interest.

Acknowledgements

Pandora data were obtained from the KORUS-AQ home pages of NASA's Goddard Space Flight Center (https://avdc.gsfc.nasa.gov/pub/DSCOVR/Pandora/DATA/KORUS-AQ/). Ground-based NO_2 MR data were obtained from Air-Korea (http://www.airkorea.or.kr/web/detailViewDown?pMENU_NO=125/). The authors would like to thank KORUS-AQ campaign team for providing the GeoTASO and Pandora data.

Funding

This work was funded by the National Institute of Environmental Research (NIER) of the Ministry of Environment [No. NIER-2021-01-01-100].

References

Boersma, K. F., Eskes, H. J., and Brinksma, E. J.: Error analysis for tropospheric NO_2 retrieval from space: ERROR ANALYSIS FOR TROPOSPHERIC NO_2, J. Geophys. Res., 109, n/a-n/a, https://doi.org/10.1029/2003JD003962, 2004.

Boersma, K. F., Eskes, H. J., Richter, A., De Smedt, I., Lorente, A., Beirle, S., van Geffen, J. H. G. M., Zara, M., Peters, E., Van Roozendael, M., Wagner, T., Maasakkers, J. D., van der A, R. J., Nightingale, J., De Rudder, A., Irie, H., Pinardi, G., Lambert, J.-C., and Compernolle, S. C.: Improving algorithms and uncertainty estimates for satellite NO_2 retrievals: results from the quality assurance for the essential climate variables (QA4ECV) project, Atmos. Meas. Tech., 11, 6651–6678, https://doi.org/10.5194/amt-11-6651-2018, 2018.

Brauer, M., Hoek, G., Van Vliet, P., Meliefste, K., Fischer, P. H., Wijga, A., Koopman, L. P., Neijens, H. J., Gerritsen, J., Kerkhof, M., Heinrich, J., Bellander, T., and Brunekreef, B.: Air Pollution from Traffic and the Development of Respiratory Infections and Asthmatic and Allergic Symptoms in Children, Am J Respir Crit Care Med, 166, 1092–1098, https://doi.org/10.1164/rccm.200108-007OC, 2002.

Burrows, J. P., Hölzle, E., Goede, A. P. H., Visser, H., and Fricke, W.: SCIAMACHY—scanning imaging absorption spectrometer for atmospheric chartography, Acta Astronautica, 35, 445–451, https://doi.org/10.1016/0094-5765(94)00278-T, 1995.

Burrows, J. P., Weber, M., Buchwitz, M., Rozanov, V., Ladstätter-Weißenmayer, A., Richter, A., DeBeek, R., Hoogen, R., Bramstedt, K., Eichmann, K.-U., Eisinger, M., and Perner, D.: The Global Ozone Monitoring Experiment (GOME): Mission Concept and First Scientific Results, 56, 151–175, https://doi.org/10.1175/1520-0469(1999)056<0151:TGOMEG>2.0.CO;2, 1999.

BYUN, D.: Science algorithms of the EPA Models-3 Community Multiscale Air Quality (CMAQ) Modeling System, 1999.

Byun, D. and Schere, K. L.: Review of the Governing Equations, Computational Algorithms, and Other Components of the Models-3 Community Multiscale Air Quality (CMAQ) Modeling System, Appl. Mech. Rev., 59, 51, https://doi.org/10.1115/1.2128636, 2006.

Callies, J., Corpaccioli, E., Eisinger, M., Hahne, A., and Lefebvre, A.: GOME-2-Metop's second-generation sensor for operational ozone monitoring, ESA Bull, 1, 28–36, 2000.

Castellanos, P., Boersma, K. F., Torres, O., and de Haan, J. F.: OMI tropospheric NO_2 air mass factors over South America: effects of biomass burning aerosols, Atmos. Meas. Tech., 8, 3831–3849, https://doi.org/10.5194/amt-8-3831-2015, 2015.

Chance, K. and Kurucz, R. L.: An improved high-resolution solar reference spectrum for earth's atmosphere measurements in the ultraviolet, visible, and near infrared, Journal of Quantitative Spectroscopy and Radiative Transfer, 111, 1289–1295, https://doi.org/10.1016/j.jqsrt.2010.01.036, 2010.

Chance, K. V. and Spurr, R. J. D.: Ring effect studies: Rayleigh scattering, including molecular parameters for rotational Raman scattering, and the Fraunhofer spectrum, Appl. Opt., 36, 5224, https://doi.org/10.1364/AO.36.005224, 1997.

Choi, S., Lamsal, L. N., Follette-Cook, M., Joiner, J., Krotkov, N. A., Swartz, W. H., Pickering, K. E., Loughner, C. P., Appel, W., Pfister, G., Saide, P. E., Cohen, R. C., Weinheimer, A. J., and Herman, J. R.: Assessment of NO_2 observations during DISCOVER-AQ and KORUS-AQ field campaigns, Atmos. Meas. Tech., 13, 2523–2546, https://doi.org/10.5194/amt-13-2523-2020, 2020.

Choi, W. J.: Introducing the geostationary environment monitoring spectrometer, J. Appl. Rem. Sens., 12, 1, https://doi.org/10.1117/1.JRS.12.044005, 2018.

Choi, M., Lim, H., Kim, J., Lee, S., Eck, T. F., Holben, B. N., Garay, M. J., Hyer, E. J., Saide, P. E., and Liu, H.: Validation, comparison, and integration of GOCI, AHI, MODIS, MISR, and VIIRS aerosol optical depth over East Asia during the 2016 KORUS-AQ campaign, Atmospheric Measurement Techniques, 12(8), 4619-4641, https://doi.org/10.5194/amt-12-4619-2019, 2019.

Chong, H., Lee, S., Kim, J., Jeong, U., Li, C., Krotkov, N. A., Nowlan, C. R., Al-Saadi, J. A., Janz, S. J., Kowalewski, M. G., Ahn, M.-H., Kang, M., Joiner, J., Haffner, D. P., Hu, L., Castellanos, P., Huey, L. G., Choi, M., Song, C. H., Han, K. M., and Koo, J.-H.: High-resolution mapping of SO2 using airborne observations from the GeoTASO instrument during the KORUS-AQ field study: PCA-based vertical column retrievals, Remote Sensing of Environment, 241, 111725, https://doi.org/10.1016/j.rse.2020.111725, 2020.

Choo, G.-H., Seo, J., Yoon, J., Kim, D.-R., and Lee, D.-W.: Analysis of long-term (2005–2018) trends in tropospheric NO_2 percentiles over Northeast Asia, Atmospheric Pollution Research, 11, 1429–1440, https://doi.org/10.1016/j.apr.2020.05.012, 2020.

Danckaert, T., Fayt, C., Van Roozendael, M., De Smedt, I., Letocart, V., Merlaud, A., and Pinardi, G.: QDOAS Software user manual, Belgian Institute for Space Aeronomy, 2016.

de Foy, B., Lu, Z., and Streets, D. G.: Satellite NO_2 retrievals suggest China has exceeded its NOx reduction goals from the twelfth Five-Year Plan, Sci Rep, 6, 35912, https://doi.org/10.1038/srep35912, 2016.

General, S., Pöhler, D., Sihler, H., Bobrowski, N., Frieß, U., Zielcke, J., Horbanski, M., Shepson, P. B., Stirm, B. H., Simpson, W. R., Weber, K., Fischer, C., and Platt, U.: The Heidelberg Airborne Imaging DOAS Instrument (HAIDI) - a novel imaging DOAS device for 2-D and 3-D imaging of trace gases and aerosols, Atmos. Meas. Tech., 7, 3459–3485, https://doi.org/10.5194/amt-7-3459-2014, 2014.

Guenther, A., Karl, T., Harley, P., Wiedinmyer, C., Palmer, P. I., and Geron, C.: Estimates of global terrestrial isoprene emissions using MEGAN (Model of Emissions of Gases and Aerosols from Nature), Atmos. Chem. Phys., 6, 3181–3210, https://doi.org/10.5194/acp-6-3181-2006, 2006.

Guenther, A. B., Jiang, X., Heald, C. L., Sakulyanontvittaya, T., Duhl, T., Emmons, L. K., and Wang, X.: The Model of Emissions of Gases and Aerosols from Nature version 2.1 (MEGAN2.1): an extended and updated framework for modeling biogenic emissions, Geosci. Model Dev., 5, 1471–1492, https://doi.org/10.5194/gmd-5-1471-2012, 2012.

Herman, J., Cede, A., Spinei, E., Mount, G., Tzortziou, M., and Abuhassan, N.: NO_2 column amounts from ground-based Pandora and MFDOAS spectrometers using the direct-sun DOAS technique: Intercomparisons and application to OMI validation, J. Geophys. Res., 114, D13307, https://doi.org/10.1029/2009JD011848, 2009.

Herman, J., Spinei, E., Fried, A., Kim, J., Kim, J., Kim, W., Cede, A., Abuhassan, N., and Segal-Rozenhaimer, M.: NO_2 and HCHO measurements in Korea from 2012 to 2016 from Pandora spectrometer instruments compared with OMI retrievals and with aircraft measurements during the KORUS-AQ campaign, Atmos. Meas. Tech., 11, 4583–4603, https://doi.org/10.5194/amt-11-4583-2018, 2018.

Hong, H., Lee, H., Kim, J., Jeong, U., Ryu, J., and Lee, D.: Investigation of Simultaneous Effects of Aerosol Properties and Aerosol Peak Height on the Air Mass Factors for Space-Borne NO_2 Retrievals, Remote Sensing, 9, 208, https://doi.org/10.3390/rs9030208, 2017.

Jeong, U., and H. Hong: Assessment of tropospheric concentrations of NO_2 from the TROPOMI/Sentinel-5 Precursor for the estimation of long-term exposure to surface NO_2 over South Korea, Remote Sensing, 13, 1877, https://doi.org/10.3390/rs13101877, 2021a.

Jeong, U., and H. Hong: Comparison of total column and surface mixing ratio of carbon monoxide derived from the TROPOMI/Sentinel-5 Precursor with In-Situ measurements from extensive ground-based network over South Korea, Remote Sensing, 13, 3987, https://doi.org/10.3390/rs13193987, 2021b.

Judd, L. M., Al-Saadi, J. A., Valin, L. C., Pierce, R. B., Yang, K., Janz, S. J., Kowalewski, M. G., Szykman, J. J., Tiefengraber, M., and Mueller, M.: The Dawn of Geostationary Air Quality Monitoring: Case Studies From Seoul and Los Angeles, Front. Environ. Sci., 6, 85, https://doi.org/10.3389/fenvs.2018.00085, 2018.

Judd, L. M., Al-Saadi, J. A., Janz, S. J., Kowalewski, M. G., Pierce, R. B., Szykman, J. J., Valin, L. C., Swap, R., Cede, A., Mueller, M., Tiefengraber, M., Abuhassan, N., and Williams, D.: Evaluating the impact of spatial resolution on tropospheric NO_2 column comparisons within urban areas using high-resolution airborne data, Atmos. Meas. Tech., 12, 6091–6111, https://doi.org/10.5194/amt-12-6091-2019, 2019.

Judd, L. M., Al-Saadi, J. A., Szykman, J. J., Valin, L. C., Janz, S. J., Kowalewski, M. G., Eskes, H. J., Veefkind, J. P., Cede, A., Mueller, M., Gebetsberger, M., Swap, R., Pierce, R. B., Nowlan, C. R., Abad, G. G., Nehrir, A., and Williams, D.: Evaluating Sentinel-5P TROPOMI tropospheric NO_2 column densities with airborne and Pandora spectrometers near New York City and Long Island Sound, Atmos. Meas. Tech., 13, 6113–6140, https://doi.org/10.5194/amt-13-6113-2020, 2020.

Kendrick, C. M., Koonce, P., and George, L. A.: Diurnal and seasonal variations of NO, NO_2 and $PM_{2.5}$ mass as a function of traffic volumes alongside an urban arterial, Atmospheric Environment, 122, 133–141, https://doi.org/10.1016/j.atmosenv.2015.09.019, 2015.

Kim, D., Lee, H., Hong, H., Choi, W., Lee, Y., and Park, J.: Estimation of Surface NO_2 Volume Mixing Ratio in Four Metropolitan Cities in Korea Using Multiple Regression Models with OMI and AIRS Data, Remote Sensing, 9, 627, https://doi.org/10.3390/rs9060627, 2017.

Kim, J., Jeong, U., Ahn, M.-H., Kim, J. H., Park, R. J., Lee, H., Song, C. H., Choi, Y.-S., Lee, K.-H., Yoo, J.-M., Jeong, M.-J., Park, S. K., Lee, K.-M., Song, C.-K., Kim, S.-W., Kim, Y. J., Kim, S.-W., Kim, M., Go, S., Liu, X., Chance, K., Chan Miller, C., Al-Saadi, J., Veihelmann, B., Bhartia, P. K., Torres, O., Abad, G. G., Haffner, D. P., Ko, D. H., Lee, S. H., Woo, J.-H., Chong, H., Park, S. S., Nicks, D., Choi, W. J., Moon, K.-J., Cho, A., Yoon, J., Kim, S., Hong, H., Lee, K., Lee, H., Lee, S., Choi, M., Veefkind, P., Levelt, P. F., Edwards, D. P., Kang, M., Eo, M., Bak, J., Baek, K., Kwon, H.-A., Yang, J., Park, J., Han, K. M., Kim, B.-R., Shin, H.-W., Choi, H., Lee, E., Chong, J., Cha, Y., Koo, J.-H., Irie, H., Hayashida, S., Kasai, Y., Kanaya, Y., Liu, C., Lin, J., Crawford, J. H., Carmichael, G. R., Newchurch, M. J., Lefer, B. L., Herman, J. R., Swap, R. J., Lau, A. K. H., Kurosu, T. P., Jaross, G., Ahlers, B., Dobber, M., McElroy, C. T., and Choi, Y.: New Era of Air Quality Monitoring from Space: Geostationary Environment Monitoring Spectrometer (GEMS), 101, E1–E22, https://doi.org/10.1175/BAMS-D-18-0013.1, 2020.

Kley, D. and McFarland, M.: Chemiluminescence detector for NO and NO_2, Atmos. Technol.; (United States), 12, 1980.

Kowalewski, M. G. and Janz, S. J.: Remote sensing capabilities of the GEO-CAPE airborne simulator, SPIE Optical Engineering + Applications, San Diego, California, United States, 92181I, https://doi.org/10.1117/12.2062058, 2014.

Kowalewski, M.G., Janz, S., Al-Saadi, J.A., Good, W., Ruppert, L., Cole, J.: GeoTASO instrument characterization and level1b radiance product generation, In: Proceedings of the 1st KORUS-AQ Science Team Meeting, Jeju, South Korea, 27 February–3 March 2017, 13. 2017

Lamsal, L. N., Martin, R. V., Parrish, D. D., and Krotkov, N. A.: Scaling Relationship for NO_2 Pollution and Urban Population Size: A Satellite Perspective, Environ. Sci. Technol., 47, 7855–7861, https://doi.org/10.1021/es400744g, 2013.

Lamsal, L. N., Janz, S. J., Krotkov, N. A., Pickering, K. E., Spurr, R. J. D., Kowalewski, M. G., Loughner, C. P., Crawford, J. H., Swartz, W. H., and Herman, J. R.: High-resolution NO_2 observations from the Airborne Compact Atmospheric Mapper: Retrieval and validation, J. Geophys. Res. Atmos., 122, 1953–1970, https://doi.org/10.1002/2016JD025483, 2017.

Latza, U., Gerdes, S., and Baur, X.: Effects of nitrogen dioxide on human health: Systematic review of experimental and epidemiological studies conducted between 2002 and 2006, International Journal of Hygiene and Environmental Health, 212, 271–287, https://doi.org/10.1016/j.ijheh.2008.06.003, 2009.

Lee, K., Yu, J., Lee, S., Park, M., Hong, H., Park, S. Y., Choi, M., Kim, J., Kim, Y., Woo, J.-H., Kim, S.-W., and Song, C. H.: Development of Korean Air Quality Prediction System version 1 (KAQPS v1) with focuses on practical issues, Geosci. Model Dev., 13, 1055–1073, https://doi.org/10.5194/gmd-13-1055-2020, 2020.

Leitão, J., Richter, A., Vrekoussis, M., Kokhanovsky, A., Zhang, Q. J., Beekmann, M., and Burrows, J. P.: On the improvement of NO_2 satellite retrievals–aerosol impact on the airmass factors, Atmos. Meas. Tech., 3, 475–493, https://doi.org/10.5194/amt-3-475-2010, 2010.

Leitch, J. W., Delker, T., Good, W., Ruppert, L., Murcray, F., Chance, K., Liu, X., Nowlan, C., Janz, S. J., Krotkov, N. A., Pickering, K. E., Kowalewski, M., and Wang, J.: The GeoTASO airborne spectrometer project, SPIE Optical Engineering + Applications, San Diego, California, United States, 92181H, https://doi.org/10.1117/12.2063763, 2014.

Levelt, P. F., van den Oord, G. H. J., Dobber, M. R., Malkki, A., Huib Visser, Johan de Vries, Stammes, P., Lundell, J. O. V., and Saari, H.: The ozone monitoring instrument, IEEE Trans. Geosci. Remote Sensing, 44, 1093–1101, https://doi.org/10.1109/TGRS.2006.872333, 2006.

Lorente, A., Folkert Boersma, K., Yu, H., Dörner, S., Hilboll, A., Richter, A., Liu, M., Lamsal, L. N., Barkley, M., De Smedt, I., Van Roozendael, M., Wang, Y., Wagner, T., Beirle, S., Lin, J.-T., Krotkov, N., Stammes, P., Wang, P., Eskes, H. J., and Krol, M.: Structural uncertainty in air mass factor calculation for NO_2 and HCHO satellite retrievals, Atmos. Meas. Tech., 10, 759–782, https://doi.org/10.5194/amt-10-759-2017, 2017.

Ma, J. Z., Beirle, S., Jin, J. L., Shaiganfar, R., Yan, P., and Wagner, T.: Tropospheric NO_2 vertical column densities over Beijing: results of the first three years of ground-based MAX-DOAS measurements (2008–2011) and satellite validation, Atmos. Chem. Phys., 13, 1547–1567, https://doi.org/10.5194/acp-13-1547-2013, 2013.

Malm, W. C. and Hand J. L.: An examination of the physical and optical properties of aerosols collected in the IMPROVE program, Atmospheric Environment, 41, 3407–3427, https://doi.org/10.1016/j.atmosenv.2006.12.012, 2007.

Merlaud, A., Constantin, D., Mingireanu, F., Mocanu, I., Maes, J., Fayt, C., Voiculescu, M., Murariu, G., Georgescu, L., Van Roozendael, M.: Small whiskbroom imager for atmospheric composition monitoring (SWING) from an unmanned aerial vehicle (UAV), in: Proceedings of the 21st ESA Symposium on European Rocket & Balloon Programmes and related Research, Thun, Switzerland pp.9–13, 2013.

Meier, A. C., Schönhardt, A., Bösch, T., Richter, A., Seyler, A., Ruhtz, T., Constantin, D.-E., Shaiganfar, R., Wagner, T., Merlaud, A., Van Roozendael, M., Belegante, L., Nicolae, D., Georgescu, L., and Burrows, J. P.: High-resolution airborne imaging DOAS measurements of NO_2 above Bucharest during AROMAT, Atmos. Meas. Tech., 10, 1831–1857, https://doi.org/10.5194/amt-10-1831-2017, 2017.

Merlaud, A., Tack, F., Constantin, D., Georgescu, L., Maes, J., Fayt, C., Mingireanu, F., Schuettemeyer, D., Meier, A. C., Schönardt, A., Ruhtz, T., Bellegante, L., Nicolae, D., Den Hoed, M., Allaart, M., and Van Roozendael, M.: The Small

Whiskbroom Imager for atmospheric compositioN monitorinG (SWING) and its operations from an unmanned aerial vehicle (UAV) during the AROMAT campaign, Atmos. Meas. Tech., 11, 551–567, https://doi.org/10.5194/amt-11-551-2018, 2018.

Nowlan, C. R., Liu, X., Leitch, J. W., Chance, K., González Abad, G., Liu, C., Zoogman, P., Cole, J., Delker, T., Good, W., Murcray, F., Ruppert, L., Soo, D., Follette-Cook, M. B., Janz, S. J., Kowalewski, M. G., Loughner, C. P., Pickering, K. E., Herman, J. R., Beaver, M. R., Long, R. W., Szykman, J. J., Judd, L. M., Kelley, P., Luke, W. T., Ren, X., and Al-Saadi, J. A.: Nitrogen dioxide observations from the Geostationary Trace gas and Aerosol Sensor Optimization (GeoTASO) airborne instrument: Retrieval algorithm and measurements during DISCOVER-AQ Texas 2013, Atmos. Meas. Tech., 9, 2647–2668, https://doi.org/10.5194/amt-9-2647-2016, 2016.

National Institute of Environmental Research (NIER) and National Aeronautics and Space Administration (NASA): KORUS-AQ Final Science Synthesis Report, available at https://espo.nasa.gov/sites/default/files/documents/5858211.pdf, last access: 27 June 2022, 2020.

Nowlan, C. R., Liu, X., Leitch, J. W., Chance, K., A., González Abad, Liu, C., Zoogman, P., Cole, J., Delker, T., Good, W., Murcray, F., Ruppert, L., Soo, D., Follette-Cook, M. B., Janz, S. J., Kowalewski, M. G., Loughner, C. P., Pickering,K. E., Herman, J. R., Beaver, M. R., Long, R. W., Szykman, J. J., Judd, L. M., Kelley, P., Luke, W. T., Ren, W., and Sl-Saadi, J. A.: Nitrogen dioxide observations from the Geostationary Trace gas and Aerosol Sensor Optimization (GeoTASO) airborne instrument: Retrieval algorithm and measurements during DISCOVER-AQ Texas 2013, Atmos. Meas. Tech., 9, 2647-2668, http://doi.org/10.5194/atm-9-2647-2016, 2016.

Nowlan, C. R., Liu, X., Janz, S. J., Kowalewski, M. G., Chance, K., Follette-Cook, M. B., Fried, A., González Abad, G., Herman, J. R., Judd, L. M., Kwon, H.-A., Loughner, C. P., Pickering, K. E., Richter, D., Spinei, E., Walega, J., Weibring, P., and Weinheimer, A. J.: Nitrogen dioxide and formaldehyde measurements from the GEOstationary Coastal and Air Pollution Events (GEO-CAPE) Airborne Simulator over Houston, Texas, Atmos. Meas. Tech., 11, 5941–5964, https://doi.org/10.5194/amt-11-5941-2018, 2018.

Palmer, P. I., Jacob, D. J., Chance, K., Martin, R. V., Spurr, R. J. D., Kurosu, T. P., Bey, I., Yantosca, R., Fiore, A., and Li, Q.: Air mass factor formulation for spectroscopic measurements from satellites: Application to formaldehyde retrievals from the Global Ozone Monitoring Experiment, J. Geophys. Res., 106, 14539–14550, https://doi.org/10.1029/2000JD900772, 2001.

Pastel, M., Pommereau, J.-P., Goutail, F., Richter, A., Pazmiño, A., Ionov, D., and Portafaix, T.: Construction of merged satellite total O_3 and NO_2 time series in the tropics for trend studies and evaluation by comparison to NDACC SAOZ measurements, Atmos. Meas. Tech., 7, 3337–3354, https://doi.org/10.5194/amt-7-3337-2014, 2014.

Platt, U.: Differential absorption spectroscopy (DOAS), Chem. Anal. Series, 127, 27–83, 1994.

Platt, U., Stutz, J.: Differential absorption spectroscopy, in: Differential Optical Absorption Spectroscopy, Springer, Berlin, Heidelberg, pp. 135–174, 2008.

Popp, C., Brunner, D., Damm, A., Van Roozendael, M., Fayt, C., and Buchmann, B.: High-resolution NO_2 remote sensing from the Airborne Prism EXperiment (APEX) imaging spectrometer, Atmos. Meas. Tech., 5, 2211–2225, https://doi.org/10.5194/amt-5-2211-2012, 2012.

Prasad, A. K., Singh, R. P., and Kafatos, M.: Influence of coal-based thermal power plants on the spatial–temporal variability of tropospheric NO_2 column over India, Environ Monit Assess, 184, 1891–1907, https://doi.org/10.1007/s10661-011-2087-6, 2012.

Qin, K., Rao, L., Xu, J., Bai, Y., Zou, J., Hao, N., Li, S., and Yu, C.: Estimating Ground Level NO_2 Concentrations over Central-Eastern China Using a Satellite-Based Geographically and Temporally Weighted Regression Model, Remote Sensing, 9, 950, https://doi.org/10.3390/rs9090950, 2017.

Richter, A., Burrows, J. P., Nüß, H., Granier, C., and Niemeier, U.: Increase in tropospheric nitrogen dioxide over China observed from space, Nature, 437, 129–132, https://doi.org/10.1038/nature04092, 2005.

Rothman, L. S., Gordon, I. E., Barber, R. J., Dothe, H., Gamache, R. R., Goldman, A., Perevalov, V. I., Tashkun, S. A., Tennyson, J. HITEMP, the high-temperature molecular spectroscopic database. Journal of Quantitative Spectroscopy and Radiative Transfer, 111(15), 2139-2150, 2010.

Schönhardt, A., Altube, P., Gerilowski, K., Krautwurst, S., Hartmann, J., Meier, A. C., Richter, A., and Burrows, J. P.: A wide field-of-view imaging DOAS instrument for two-dimensional trace gas mapping from aircraft, Atmos. Meas. Tech., 8, 5113–5131, https://doi.org/10.5194/amt-8-5113-2015, 2015.

Shah, V., Jacob, D. J., Li, K., Silvern, R. F., Zhai, S., Liu, M., Lin, J., and Zhang, Q.: Effect of changing NO_x lifetime on the seasonality and long-term trends of satellite-observed tropospheric NO_2 columns over China, Atmos. Chem. Phys., 20, 1483–1495, https://doi.org/10.5194/acp-20-1483-2020, 2020.

Skamarock, W., Klemp, J., Dudhia, J., Gill, D., Barker, D., Wang, W., Huang, X.-Y., and Duda, M.: A Description of the Advanced Research WRF Version 3, UCAR/NCAR, https://doi.org/10.5065/D68S4MVH, 2008.

Spinei, E., Whitehill, A., Fried, A., Tiefengraber, M., Knepp, T. N., Herndon, S., Herman, J. R., Müller, M., Abuhassan, N., Cede, A., Richter, D., Walega, J., Crawford, J., Szykman, J., Valin, L., Williams, D. J., Long, R., Swap, R. J., Lee, Y., Nowak, N., and Poche, B.: The first evaluation of formaldehyde column observations by improved Pandora spectrometers during the KORUS-AQ field study, Atmos. Meas. Tech., 11, 4943–4961, https://doi.org/10.5194/amt-11-4943-2018, 2018.

Spurr, R. and Christi, M.: On the generation of atmospheric property Jacobians from the (V)LIDORT linearized radiative transfer models, Journal of Quantitative Spectroscopy and Radiative Transfer, 142, 109–115, https://doi.org/10.1016/j.jqsrt.2014.03.011, 2014.

Tack, F., Merlaud, A., Iordache, M.-D., Danckaert, T., Yu, H., Fayt, C., Meuleman, K., Deutsch, F., Fierens, F., and Van Roozendael, M.: High-resolution mapping of the NO_2 spatial distribution over Belgian urban areas based on airborne APEX remote sensing, Atmos. Meas. Tech., 10, 1665–1688, https://doi.org/10.5194/amt-10-1665-2017, 2017.

Tack, F., Merlaud, A., Meier, A. C., Vlemmix, T., Ruhtz, T., Iordache, M.-D., Ge, X., van der Wal, L., Schuettemeyer, D., Ardelean, M., Calcan, A., Constantin, D., Schönhardt, A., Meuleman, K., Richter, A., and Van Roozendael, M.: Intercomparison of four airborne imaging DOAS systems for tropospheric NO_2 mapping–the AROMAPEX campaign, Atmos. Meas. Tech., 12, 211–236, https://doi.org/10.5194/amt-12-211-2019, 2019.

Tack, F., Merlaud, A., Iordache, M.-D., Pinardi, G., Dimitropoulou, E., Eskes, H., Bomans, B., Veefkind, P., and Van Roozendael, M.: Assessment of the TROPOMI tropospheric NO_2 product based on airborne APEX observations, Atmos. Meas. Tech., 14, 615–646, https://doi.org/10.5194/amt-14-615-2021, 2021.

Tzortziou, M., Parker, O., Lamb, B., Herman, J., Lamsal, L., Stauffer, R., and Abuhassan, N.: Atmospheric Trace Gas (NO_2 and O_3) Variability in South Korean Coastal Waters, and Implications for Remote Sensing of Coastal Ocean Color Dynamics, Remote Sensing, 10, 1587, https://doi.org/10.3390/rs10101587, 2018.

Valks, P., Pinardi, G., Richter, A., Lambert, J.-C., Hao, N., Loyola, D., Van Roozendael, M., and Emmadi, S.: Operational total and tropospheric NO_2 column retrieval for GOME-2, Atmos. Meas. Tech., 4, 1491–1514, https://doi.org/10.5194/amt-4-1491-2011, 2011.

Vandaele, A. C., Hermans, C., Simon, P. C., Carleer, M., Colin, R., Fally, S., Mérienne, M. F., Jenouvrier, A., and Coquart, B.: Measurements of the NO_2 absorption cross-section from 42 000 cm^{-1} to 10 000 cm^{-1} (238–1000 nm) at 220 K and 294 K, Journal of Quantitative Spectroscopy and Radiative Transfer, 59, 171–184, https://doi.org/10.1016/S0022-4073(97)00168-4, 1998.

Veefkind, J. P., Aben, I., McMullan, K., Förster, H., de Vries, J., Otter, G., Claas, J., Eskes, H. J., de Haan, J. F., Kleipool, Q., van Weele, M., Hasekamp, O., Hoogeveen, R., Landgraf, J., Snel, R., Tol, P., Ingmann, P., Voors, R., Kruizinga, B., Vink, R., Visser, H., and Levelt, P. F.: TROPOMI on the ESA Sentinel-5 Precursor: A GMES mission for global observations of the atmospheric composition for climate, air quality and ozone layer applications, Remote Sensing of Environment, 120, 70–83, https://doi.org/10.1016/j.rse.2011.09.027, 2012.

Vlemmix, T., Ge, X., de Goeij, B. T. G., van der Wal, L. F., Otter, G. C. J., Stammes, P., Wang, P., Merlaud, A., Schüttemeyer, D., Meier, A. C., Veefkind, J. P., and Levelt, P. F.: Retrieval of tropospheric NO_2 columns over Berlin from high-resolution airborne observations with the spectrolite breadboard instrument, Atmos. Meas. Tech. Discuss., https://doi.org/10.5194/amt-2017-257, in review, 2017.

Wiedinmyer, C., Quayle, B., Geron, C., Belote, A., McKenzie, D., Zhang, X., O'Neill, S., and Wynne, K. K.: Estimating emissions from fires in North America for air quality modeling, Atmospheric Environment, 40, 3419–3432, https://doi.org/10.1016/j.atmosenv.2006.02.010, 2006.

Wiedinmyer, C., Akagi, S. K., Yokelson, R. J., Emmons, L. K., Al-Saadi, J. A., Orlando, J. J., and Soja, A. J.: The Fire INventory from NCAR (FINN): a high resolution global model to estimate the emissions from open burning, Geosci. Model Dev., 4, 625–641, https://doi.org/10.5194/gmd-4-625-2011, 2011.

Wold, S., Esbensen, K., and Geladi, P.: Principal component analysis, Chemometrics and Intelligent Laboratory Systems, 2, 37–52, https://doi.org/10.1016/0169-7439(87)80084-9, 1987.

Woo, J.-H., Choi, K.-C., Kim, H. K., Baek, B. H., Jang, M., Eum, J.-H., Song, C. H., Ma, Y.-I., Sunwoo, Y., Chang, L.-S., and Yoo, S. H.: Development of an anthropogenic emission processing system for Asia using SMOKE, Atmospheric Environment, 58, 5–13, https://doi.org/10.1016/j.atmosenv.2011.10.042, 2012.

Zoogman, P., Liu, X., Suleiman, R. M., Pennington, W. F., Flittner, D. E., Al-Saadi, J. A., Hilton, B. B., Nicks, D. K., Newchurch, M. J., Carr, J. L., Janz, S. J., Andraschko, M. R., Arola, A., Baker, B. D., Canova, B. P., Chan Miller, C., Cohen, R. C., Davis, J. E., Dussault, M. E., Edwards, D. P., Fishman, J., Ghulam, A., González Abad, G., Grutter, M., Herman, J. R., Houck, J., Jacob, D. J., Joiner, J., Kerridge, B. J., Kim, J., Krotkov, N. A., Lamsal, L., Li, C., Lindfors, A., Martin, R. V., McElroy, C. T., McLinden, C., Natraj, V., Neil, D. O., Nowlan, C. R., O'Sullivan, E. J., Palmer, P. I., Pierce, R. B., Pippin, M. R., Saiz-Lopez, A., Spurr, R. J. D., Szykman, J. J., Torres, O., Veefkind, J. P., Veihelmann, B., Wang, H., Wang, J., and Chance, K.: Tropospheric emissions: Monitoring of pollution (TEMPO), Journal of Quantitative Spectroscopy and Radiative Transfer, 186, 17–39, https://doi.org/10.1016/j.jqsrt.2016.05.008, 2017.